2014

Acoustic timescale characterization of hot spot detonability

Michael D. Kurtz
Iowa State University

Recommended Citation

Kurtz, Michael D., "Acoustic timescale characterization of hot spot detonability" (2014). *Graduate Theses and Dissertations*. 13931.
https://lib.dr.iastate.edu/etd/13931

Acoustic timescale characterization of hot spot detonability

by

Michael Drew Kurtz

A thesis submitted to the graduate faculty
in partial fulfillment of the requirements for the degree of
MASTER OF SCIENCE

Major: Aerospace Engineering

Program of Study Committee:
Jonathan D. Regele, Major Professor
Alric Rothmayer
Thomas Rudolphi

Iowa State University
Ames, Iowa
2014

To my wife,
parents,
and brothers.

TABLE OF CONTENTS

LIST OF TABLES

LIST OF FIGURES

ACKNOWLEDGEMENTS

I would like to take this opportunity to express my thanks to those who helped me with various aspects of conducting research and the writing of this thesis. First and foremost, my advisor Dr. Jonathan D. Regele for his guidance, patience and support throughout this research and the writing of this thesis. His insights and encouragement have often given this work new life and inspired me to complete my graduate education.

I would also like to thank the other members of my committee members, Dr. Alric Rothmayer and Dr. Thomas Rudolphi, for their efforts and contributions to this work. I would also like to thank them for the education they have been a part of providing to me throughout my career at Iowa State University.

I thank my collegues at Iowa State University for their advice, encouragement, and friendship duing my time at ISU. This includes David Sikorski, Richard Livings, Brad Kirkpatrick, Ben Zimmerman, Alex Lee, and many others.

Finally, I must thank my wife and parents for their steadfast support and encouragement. I am especially grateful to my wife Abigail, who has endured patiently the long hours away from me. I could not have completed this work without her support and blessing.

A portion of the research within this thesis would not have been possible without the HPC equipment purchased through NSF MRI grant number CNS 1229081 and NSF CRI grant number 1205413.

ABSTRACT

Premixed reactive mixtures of fuel and oxidizer often contain regions of higher temperature. These regions of raised temperature are generally called hot spots and have been shown to be the autoignition center in reactive mixtures. Linear temperature gradients and thermal stratification are often used to characterize their behavior. In this work, hot spots are modeled as a linear temperature gradient adjacent to a constant temperature plateau. This approach retains the simplicity of a linear temperature gradient, but captures the effects of a local temperature maximum of finite size. A one-step Arrhenius reaction for H_2-Air is used to model the reactive mixture.

A one dimensional model is considered first to characterize hot spot behavior based on the relation between how quickly the fuel reacts (excitation time) and the time it takes for fluid motion to be induced (acoustic time). Plateaus of three different initial sizes spanning two orders of magnitude are simulated. Each length corresponds to a different ratio of excitation time to acoustic time or acoustic timescale ratio. It is shown that ratios less than unity react at nearly isochoric conditions while ratios greater than unity react at nearly isobaric conditions. It is demonstrated that the gasdynamic response is characterized by the *a priori* prescribed hot spot acoustic timescale ratio. Based upon this ratio, it is shown that the plateau can have either a substantial or negligible impact on the reaction of a surrounding temperature gradient. This is explored further as the slope of the temperature gradient is varied. Plateaus with a particular acoustic timescale ratio are shown to facilitate detonation formation inside gradients that would otherwise not detonate.

This 1-D model is extended to two dimensions with symmetric and asymmetric plateau regions, modeled using both rectangular and elliptical geometries. Even with clear differences in behavior between one and two dimensions, the hot spot acoustic timescale ratio is shown to characterize the 2-D gasdynamic response. The relationship between one and two dimensions is explored using asymmetric plateau regions. It is shown that 1-D behavior is recovered over a finite time. Furthermore, the duration of this 1-D behavior is directly related to the asymmetry of the plateau.

CHAPTER 1. OVERVIEW

1.1 Introduction

Combustion processes generally occur at high temperatures and relatively constant pressures. However, as reactions become more rapid, pressures are no longer small and compressibility, *i.e.*, consequential density fluctuations, plays a significant role in their genesis, evolution, and propagation. Reactions are termed detonations when the reaction is preceded by a shock wave, meaning the reaction is traveling at supersonic velocity relative to the undisturbed gas. The shock heats the reactive mixture by compression, triggering a chemical reaction. This releases energy in a fashion that reinforces and amplifies the shock, allowing this coupled system to propagate at a self-sustained rate. Oppenheim [3] states that detonations are *de facto* present in any modern combustion systems today. He referred to the formation of a detonation at a localized reaction center, or hot spot, as an "explosion in the explosion."

These hot spots can lead to the formation of a detonation wave and cause severe damage to all types of mechanical systems, from an internal combustion engine to the thrust chamber of a rocket engine or industrial diesel engine. In these cases, detonation prevention is the goal, however there is a diverse group of applications where detonations are caused intentionally. Humans have used detonations for destructive purposes from invention of gunpowder to the development of the thermonuclear warhead.

The destructive nature of detonations has also been constructively harnessed for mining and propulsion applications. Over the past several decades there has been a significant interest in the development of Pulsed Detonation Engines (PDE) and more recently Rotational Detonation Engines (RDE) due to the substantial increase in efficiency over traditional jet engines, *e.g.*, turbojets and turbofans.

Therefore, the understanding and characterization of the underlying physics of hot spots and the role they play in detonations is crucial in resolving the problems they cause and advancing technology to be more efficient and safe. To this end the primary objective of this thesis is to model, analyze, and characterize these regions of non-uniform temperature distribution within a reactive medium. The next section will provide a detailed background of this field of study, the current state of hot spots, and an introduction to the tools that will be used in this thesis.

1.2 Background

1.2.1 Detonation Phenomenon

The term *detonation* refers to a shock-induced combustion wave propagating supersonically through a reactive mixture. Detonations were first investigated experimentally in 1881 by Berthelot and Vieille [4] and Mallard and Chatelier [5]. After much investigation, mathematical predictions of the wave speed of a detonation were formulated in the early 1900's Chapman [6] and Jouguet [7] who independently stated that the behavior of a detonation is represented by the tangency point of the Rankine-Hugoniot curve. This curve, shown in Fig. 1.2.1, mathematically depicts the difference between a detonation and deflagration. For a given initial condition, the end state must fall in one of the two branches. The upper tangency point is called the upper Chapman-Jouguet (CJ) point. This CJ detonation agrees well with experimental values for detonations, but does not explain what happens immediately downstream of the discontinuity. Later, from 1940-1943, Zel'dovich [8], von Neumann [9], and Döring [10] independently formulated their 1-D model of a detonation wave (ZND model). This model assumes a non-reactive shock discontinuity, followed by an induction/reaction region which decays to the CJ state.

To better understand the structure of this phenomenon, the analytical solution to the ZND detonation model is found using the methodology outlined in Strehlow [2] and summarized in Sec. 3.1. The same detonation wave is simulated numerically with the Adaptive Wavelet-Collocation Method (AWCM) using a CJ jump condition as an initial condition. The reactive Euler equations are solved and the solution evolves from the initial CJ jump condition to a ZND

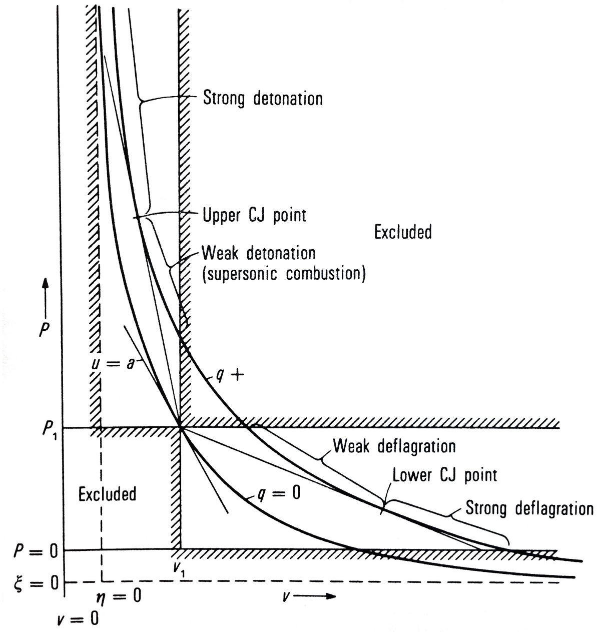

Figure 1.1 Rankine-Hugoniot curve[2]

wave propagating at the theoretical detonation speed. These numerical results are compared to the analytical solution and the effects of grid resolution are investigated.

Later, Zeldovich showed that detonations can be formed by the explosion of a nonuniformly preconditioned region of reactive mixture with a spatial gradient of ignition delay time [11]. This mechanism was first suggested in the form of a linear temperature gradient. Lee *et al.* [12, 13, 14] expanded upon this when they found evidence of the gradient mechanism in photo-initiation experiments and termed it the Shock Wave Amplification by Coherent Energy Release (SWACER) mechanism. They show that a shock wave will be amplified only if the time sequence of the energy release due to chemical reaction is in phase with the shock wave itself.

In the late 1950's and early 1960's it was discovered that detonations are truly unsteady, non-planar, multi-dimensional phenomena [15, 16, 17]. In multiple dimensions, the curvature of the detonation front competes with the energy release from the chemical reaction, making it more difficult to sustain the detonation wave [18]. However, multidimensional detonations have a cellular structure caused by a triple Mach intersection point, displayed in Fig. 1.2(a) and 1.2(b). Figure 1.2(c) demonstrates a soot-coated film, which tracks the path of these triple

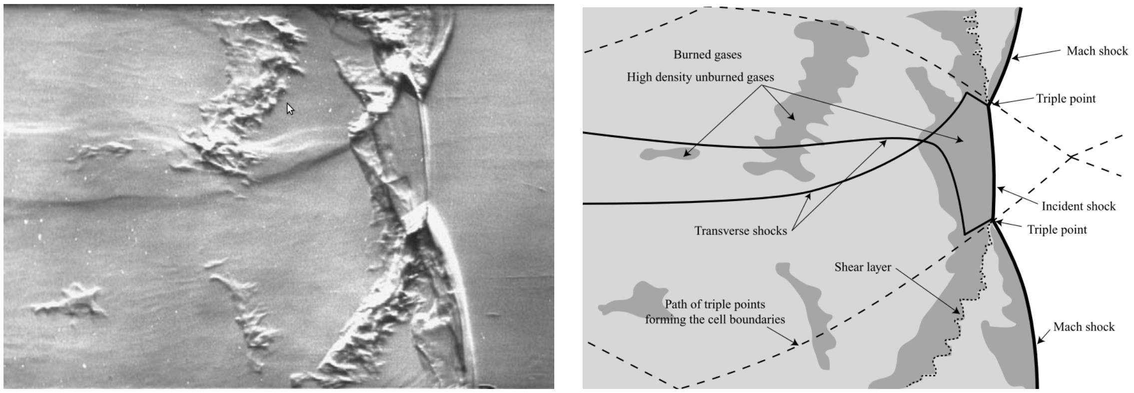

(a) Schlieren photograph of detonation cell structure[19]

(b) Sketch explaining the structures seen in (a). Two triple points can be seen very clearly [19].

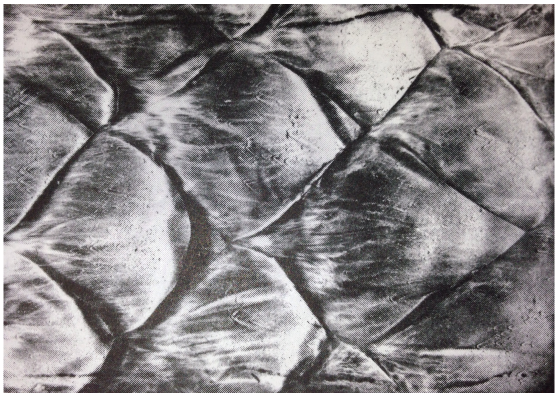

(c) Soot-coated film depicting the location of the detonation triple points after it travels through a rectangular channel

Figure 1.2 Experimental photos of detonation and explanatory sketch

points and displays the detonation's overall structure. There are a number of other methods to capture detonation structure, including OH fluorescence, open shutter photography, and schlieren photography. However, the detonations studied in this work will not develop to the point of being cellular in nature. Therefore, it is not necessary to go into more detail about the extensive amount of research that is done in the area of multi-dimensional detonation structure.

1.2.2 Hot Spots

The term hot spot generally refers to a region of fluid within a reactive mixture that is initially at a higher temperature or reactivity than its surroundings and reacts in an explosive manner. Hot spots are known to form through many different mechanisms including mechanical friction, an electrical fault in processing equipment, or a localized exothermic reaction [20]. They have also been shown to form due to pressure fluctuations generated by shock-flame interactions within a flame brush [21, 22]. Sankaran *et al.* [23, 24, 25] study the ignition of H_2-Air with a random, non-uniform initial temperature and compositional distribution in an HCCI combustion process. Based upon the initial conditions, their results show that combustion may occur in flame sheets with acoustic wave generation, or in a more volumetric fashion with strong compression waves generated at fast reaction fronts. It is of interest to investigate these hot spots to understand the hazards they pose as well as characterize their ignition and the response of the surrounding fluid.

Hot spots have been studied for several decades, specifically the role they play in detonations. Merzhanov [26], Thomas [27], and Zaturska [28] use thermal explosion theory to present critical conditions at hot spots that could lead to a detonation. Clarke [29] and Nikiforakis and Clarke [30] constructed a theoretical description of how hot spots evolve into a detonation wave by using the induction-domain equation in combination with Arrhenius kinetics. They state that hot spots can create compression waves, expansion waves, induction regions and fast flames, which all lead, in the absence of any inhibitory mechanism, to detonation.

Jackson, Kapila, and Stewart [31] investigate the evolution of two different types of localized hot spots: a wall-type reaction with a temperature gradient in the center, and an internal-type reaction that has a rounded peak. They treat the gasdynamic effects as secondary and focus on a regime that is dominated by chemical heating, resulting in an essentially constant volume explosion in both cases.

Sileem, Kassoy, and Hayashi [32] and Kassoy *et al.* [33] study the DDT process by using a spatially resolved thermal power deposition on the acoustic timescale of the deposition volume in a reactive mixture with low activation energy. The energy deposition and subsequent chemical reaction both generate compression waves that preheat the reactive medium, which transitions to a detonation. Regele *et al.* [34] extended this effort to higher activation energy reactive mixtures and found that hot spots can create minor compression waves or form spontaneous waves that ultimately form a detonation. Furthermore, it is demonstrated that the hot spot behavior can be classified in terms of the ratio of the heat release time to the acoustic timescale of the hot spot. Subsequently, Regele *et al.* [35, 36] extended the 1-D analysis to two dimensions and demonstrated that for sufficiently strong energy depositions, multidimensional behavior is quite similar to the 1-D description.

Gu, Emerson, and Bradely [37] performed numerical simulations of temperature gradients and identified five distinct modes of reaction front propagation outlined by Zeldovich [38]. This linear temperature gradient has been explored by Kapila *et al.* [39] who claim that a detonation occurs in two phases. In the first phase, the medium is preheated, and in the second phase a detonation forms. They model many different linear temperature gradients and find that shallow gradients form detonations, whereas steep gradients do not. Additionally, Sharpe and Short [40] and Liberman *et al.* [41] show that the minimum gradient length required to form a detonation using detailed kinetic models is 2-3 orders of magnitude larger than the length computed with simplified one-step reaction models. This means detailed kinetics are necessary for a quantitative prediction of critical gradient length.

1.2.3 Acoustic Timescale

The amount of time it takes for acoustic waves to propagate some characteristic length, l, through a mixture with local sound speed, a, is called the acoustic timescale, t_a. If a sufficient amount of energy is added in a time period much smaller than the acoustic time, the fluid will remain inertially confined (negligible induced fluid motion) during the reaction. If energy is added on a timescale much larger than t_a, the fluid is allowed to expand during the reaction. Energy added on the order of the acoustic time results in partial inertial confinement.

There are many papers from Clarke, Kassoy, and others [32, 42, 43, 44, 45, 46, 47] exploring problems involving thermomechanical effects caused by gas expansion due to energy addition. Energy is added over a wide range of time and length-scales through boundaries or spatial power depositions. In these works asymptotic procedures are used to find equations that describe the gasdynamic response of the fluid to this energy addition. They show that the pressure response due to energy addition is highly dependent upon the strength of the power deposition. These works have all contributed to developing a systematic approach that describes the thermomechanical response to a thermal disturbance. They demonstrate that detonations are produced depending on either the amount of energy added in a certain time or how quickly a sufficient amount of energy is added.

Kassoy [48] performed a formal asymptotic acoustic timescale analysis of the Navier-Stokes equations, describing the response of an inert compressible gas to relatively large, transient, spatially resolved, energy addition into a finite volume. He defines the ratio of the heating time to the local acoustic time and uses this parameter to characterize the thermomechanical response to energy addition during a finite heating period. When the heat addition is small compared to the internal energy of the gas, acoustic waves propagate into the surroundings. In contrast, a large heat addition during the heating period sends shock waves into the surroundings. When the heat addition is sufficiently large, the fluid response creates high pressure gas, which can cause shock waves. Kassoy [49] also studied the thermomechanical response of a reactive gas to a transient, spatially distributed thermal energy addition. He showed that the induced Mach number can range from asymptotically small to supersonic, depending upon the energy added during the heating timescale. The range of responses due to this induced velocity vary from weak acoustic waves to blast waves.

Recently, Kassoy [50] did a similar study to analyze the thermomechanical response of a supercritical reactive fluid, heated by a spatially distributed, transient power deposition source to show that compressive mechanical disturbances propagating into unheated pockets of reactive gas can act as sources of ignition. Additionally, Regele [51] showed that the reaction of a fuel pocket surrounded by combustion products can be characterized by the acoustic timescale. This timescale can be used to estimate the pocket's impact on the surroundings.

1.2.4 Objectives and Organization

As discussed above, fundamental insight into autoignition hot spot behavior and detonation initiation is often studied with linear temperature gradients [37, 39, 40, 41]. However, real hot spots rarely take this form. Normally they take the shape of some curve, with a local maximum [23, 24, 25, 52]. The current work models a hot spot as a temperature gradient adjacent to a temperature plateau. Figure 1.3 illustrates this model hot spot. The plateau region is designed to mimic the local temperature maximum and the surrounding temperature

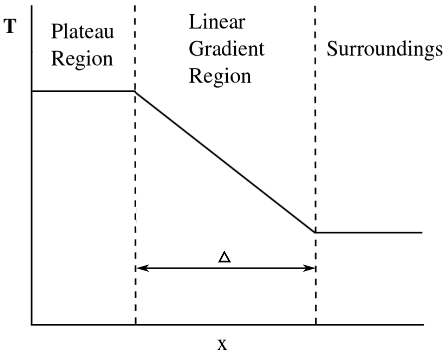

Figure 1.3 Initial temperature distribution for a generalized hot spot model

gradient region. With this generalized model, it becomes possible to analyze the impact of the plateau's reaction on the surrounding reactive mixture.

The objective of the proposed work is to study the effect of a constant temperature plateau region on the surrounding linear temerature gradient in terms of the acoustic timescale ratio. Three different 1-D approaches are considered to characterize the fluid response with the excitation and acoustic timescales of the plateau region. First we examine the case with a plateau and no temperature gradient. Three plateau lengths with different acoustic timescale ratios are used to demonstrate the entire spectrum of fluid responses. Second, these plateau regions are combined with a linear temperature gradient to determine their effect on the reaction of the gradient region. Third, a parametric study of plateau length and temperature gradients are performed in order to understand how different plateau sizes affect the detonability of different temperature gradients.

Although the one-dimensional hot spot model provides fundamental insight, hot spots are inherently multidimensional and expansion waves propagate in different directions. Therefore, this thesis will also extend the hot spot model to multiple dimensions and demonstrate how multidimensional effects modify the behavior of the hot spot model. To this end, two 2-D models will be used to investigate the effect of a constant temperature plateau on a surrounding gradient. First, a rectangular, constant temperature plateau region surrounded by a linear temperature gradient will be implemented as a direct extension of the 1-D model. For these cases, the expansion waves generated by the plateau reaction will be orthogonal to each other and nearly planar along the axes at early times. Eventually, the expansion waves merge, forming one wave which reaches the center in roughly the acoustic time of the reaction products. It is anticipated that until this time the behavior along the x- and y-axes will be very similar to the 1-D model results. The second model, accounting for curvature effects seen in real systems, will feature an elliptic plateau region surrounded by a linear temperature gradient. Unlike the rectangular cases, expansion waves will reduce the pressure and temperature on the axes from the moment the reaction begins.

This thesis will be organized as follows. The mathematical models used to perform the simulations along with the important timescales needed for modeling the problems are presented in Chapter 2. These problem models are described in Chapter 3, followed by the numerical method used to solve them in Chapter 4. Finally, the results and conlusions are presented in Chapters 5 and 6.

CHAPTER 2. METHODOLOGY

2.1 Mathematical Model

The general governing equations for this flow are the reactive Navier-Stokes equations. Since the current focus is on auto-ignition, spontaneous waves, and the interaction between these phenomena, transport effects are negligible, which is shown explicitly in the next two sections. Since the focus of this study is to characterize the thermomechanical response of surrounding fluid to the reaction of a localized plateau region, a simple one-step reaction model is employed. While detailed chemistry is necessary to quantitatively predict the critical gradient length required for detonation formation [40, 41], this is not the objective of the current work. Thus, the reactive Euler equations with a one-step Arrhenius reaction are used to model the reactive mixture. Written in conservative vector form, the 2-D reactive Euler equations are

$$\frac{\partial U'}{\partial t'} + \frac{\partial F'_x(U')}{\partial x'} + \frac{\partial F'_y(U')}{\partial y'} = S', \tag{2.1}$$

where

$$U' = \left\{ \begin{array}{c} \rho' \\ \rho' u' \\ \rho' v' \\ \rho' e'_T \\ \rho' Y' \end{array} \right\}, \; F'_x = \left\{ \begin{array}{c} \rho u' \\ \rho u'^2 + p' \\ \rho u' v' \\ (\rho e'_T + p') u' \\ \rho Y u' \end{array} \right\}, \; F'_y = \left\{ \begin{array}{c} \rho' v' \\ \rho' u' v' \\ \rho' v'^2 + p' \\ (\rho' e'_T + p') v' \\ \rho' Y v' \end{array} \right\}, \; S' = \left\{ \begin{array}{c} 0 \\ 0 \\ 0 \\ 0 \\ -\dot{W}' \end{array} \right\}. \tag{2.2}$$

Here ρ' is the density, $\rho' u'$ is the x-momentum, $\rho' v'$ is the y-momentum, e'_T is the total energy, Y is the fuel mass fraction, and the primes denote dimensional values. The total energy is defined as the sum of internal, kinetic, and chemical energy, expressed as

$$e'_T = \frac{p'}{\rho'(\gamma - 1)} + \frac{1}{2}(u'^2 + v'^2) + Yq' \tag{2.3}$$

Variable name	Nondimensionalization
Position	$x = x'/l'$
Time	$t = t'a'_o/l'$
Velocity	$u = u'/a'_o$
Pressure	$p = p'/\gamma p'_o = p'/\rho'_o a'^2_o$
Density	$\rho = \rho'/\rho'_o$
Temperature	$T = T'/\gamma T'_o$
Total Energy	$e_t = e'_t/a'^2_o$
Activation Energy	$E_a = E'_a/a'^2_o = E'_a/\gamma R'T'_o$
Heat of Reaction	$q = q'/a'^2_o$
External Power Deposition	$\dot{Q} = \dot{Q}'t'_a/\rho'_o a'^2_o$
Reaction Rate	$\dot{W} = \dot{W}'t'_a/\rho'_o$
Pre-exponential Factor	$B = B'l'/a'_o$

Table 2.1 Nondimensional variable definitions (Primes denote dimensional quantities.)

The reaction rate is given by

$$\dot{W}' = B'\rho' Y e^{-E'_a/R'T'}, \tag{2.4}$$

with the pre-exponential factor B', heat of reaction q', activation energy E'_a. Temperature is found with the ideal gas law, $p' = \rho' R' T'$.

Since the wavelet approach requires all flow variables to be $O(1)$, the governing equations must be nondimensionalized. The variables chosen to nondimensionalize the above equations are presented in Table 2.1. The spatial coordinate x is nondimensionalized by an arbitrary length l'. The reference sound speed $a'^2_o = \gamma R' T'_o$ is used to nondimensionalize energy. The explicit derivation of the nondimentionalization for the reactive Euler equations, *i.e.*, the mass, momentum, energy, and species conservation equations, in addition to the state equation, sound speed, and internal energy is outlined in Appendix A. Written in conservative vector form, the nondimensional 2-D reactive Euler equations are

$$\frac{\partial U}{\partial t} + \frac{\partial F_x(U)}{\partial x} + \frac{\partial F_y(U)}{\partial y} = S, \tag{2.5}$$

where

$$U = \left\{ \begin{array}{c} \rho \\ \rho u \\ \rho v \\ \rho e_T \\ \rho Y \end{array} \right\}, \; F_x = \left\{ \begin{array}{c} \rho u \\ \rho u^2 + p \\ \rho u v \\ (\rho e_T + p)u \\ \rho Y u \end{array} \right\}, \; F_y = \left\{ \begin{array}{c} \rho v \\ \rho u v \\ \rho v^2 + p \\ (\rho e_T + p)v \\ \rho Y v \end{array} \right\}, \; S = \left\{ \begin{array}{c} 0 \\ 0 \\ 0 \\ 0 \\ -\dot{W} \end{array} \right\}. \tag{2.6}$$

The total energy and reaction rate become

$$e_T = \frac{p}{\rho(\gamma - 1)} + \frac{1}{2}(u^2 + v^2) + Yq \tag{2.7}$$

and

$$\dot{W} = B\rho Y e^{-E_a/T} \tag{2.8}$$

respectively. The state equation reduces to $p = \rho T$. The nondimensional equations are solved for all simulations in this work. Since the ZND model is used as a verification test case, the results are presented in nondimensional units. In order to make the results more applicable to a wider audience, the hot spot results are presented either in dimensioned or some other normalized form.

For use in the 1-D simulations, these reduce to the nondimensional 1-D reactive Euler equations, given by

$$\frac{\partial U}{\partial t} + \frac{\partial F_x(U)}{\partial x} = S, \tag{2.9}$$

with

$$U = \left\{ \begin{array}{c} \rho \\ \rho u \\ \rho e_T \\ \rho Y \end{array} \right\}, \; F_x = \left\{ \begin{array}{c} \rho u \\ \rho u^2 + p \\ (\rho e_T + p)u \\ \rho Y u \end{array} \right\}, \; S = \left\{ \begin{array}{c} 0 \\ 0 \\ 0 \\ -\dot{W} \end{array} \right\} \tag{2.10}$$

and energy equation

$$e_T = \frac{p}{\rho(\gamma - 1)} + \frac{1}{2}u^2 + Yq. \tag{2.11}$$

2.2 Length and Timescale Definitions

The amount of time it takes a reactive mixture to be consumed (excitation time) and the time it takes for fluid motion to be induced (acoustic time) have been successfully used to characterize a number of reactive thermomechanical problems [49, 34]. The relationship between these two time scales determines the process by which the mixture reacts and the effect it will have upon its surroundings.

Consider a volume of premixed, reactive mixture at some initial temperature and pressure. The half-reaction time, τ_r, is the time at which the fuel mass fraction $Y = 0.5$. The excitation time, τ_e, is defined roughly as the time it takes for the fuel to be consumed. The consumption of the fuel does not have exact start and end times, so the excitation time needs to be approximated. Thus, the slope of the fuel mass fraction when half the fuel has been consumed, $dY_{(Y=0.5)}/dt$, is used to linearly extrapolate the start and end times, the difference of which is defined to be the excitation time. The ignition delay time, τ_i, is the time it takes for the reaction to begin and is defined as $\tau_i = \tau_r - \tau_e/2$.

The amount of time it takes for mechanical disturbances, such as expansion waves, to propagate some characteristic length l through a mixture with local sound speed a is termed the acoustic timescale, given by

$$t_a = \frac{l}{a}. \tag{2.12}$$

As in previous work [33, 48, 34], an acoustic timescale ratio can be defined as

$$\frac{\tau_e}{t_a} = \frac{\tau_e a}{l} = \frac{L}{l}, \tag{2.13}$$

where the acoustic reaction length is defined as $L = \tau_e \cdot a$ and τ_e is chosen as the isochoric excitation time, τ_e^v. This ratio can then be used to characterize the results. Ratios greater than one will result in weak acoustic wave generation, ratios less than one can generate strong compression waves, and those roughly equal to one generate compression between these two delineating behaviors. The characteristic length,

$$l = \frac{L}{\tau_e/t_a}, \tag{2.14}$$

can be determined from a prescribed acoustic timescale ratio.

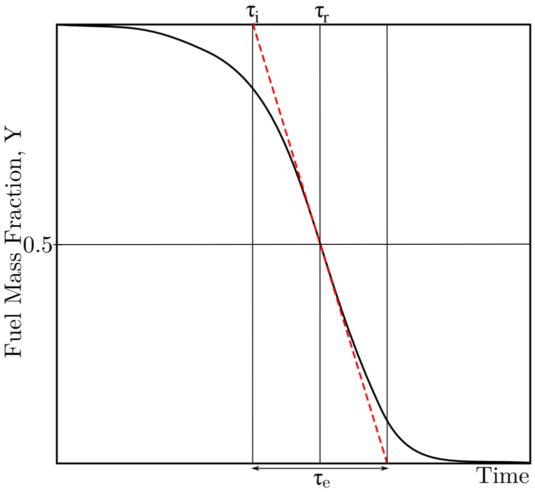

Figure 2.1 Visual depiction of the excitation time τ_e, ignition delay time τ_i, and half-reaction time τ_r. The red, dashed line is a linear extrapolation of the fuel mass fraction at Y=0.5. This is used to define the excitation time.

The viscous and conductive timescales, defined by Kassoy [48] and rewritten in terms of acoustic Reynolds number, $Re_a = la_o/\nu_o$, and Prandtl number, $Pr = \nu_o/\kappa_o$, are expressed as

$$\tau_v = \frac{l^2}{\nu_o} = Re_a t_a \tag{2.15}$$

and

$$\tau_c = \frac{l^2}{\kappa_o} = Re_a Pr t_a. \tag{2.16}$$

Here, ν_o and κ_o as the characteristic dynamic viscosity and thermal diffusivity. These relations show that the timescale ratios associated with molecular transport to acoustic timescales are proportional to Re_a.

Common combustion systems typically have $Re_a = O(10^4)$ and Prandtl numbers of 0.7. Equations 2.15 and 2.16 demonstrate the acoustic timescale is four orders of magnitude smaller than τ_v and τ_c. This suggests that transport effects are negligible and the flow can be modeled using the reactive Euler equations.

CHAPTER 3. PROBLEM STATEMENT

The problems described in this thesis are complex in nature, resulting in the formation of detonations in some instances. Therefore, it is necessary to provide some insight into detonations and their structure. To this end, the ZND detonation model, the simplest detonation model including a finite reaction rate, will be presented. It will be used in Chapter 4 to validate the numerical methods used with analytical results. After the ZND model, 1-D and 2-D models used in this work are described.

3.1 ZND Detonation Model

Consider a fully established detonation traveling through a reactive mixture at speed D. Figure 3.1 shows the transformation between the shock stationary (denoted by superscript $*$) and shock moving (lab) reference frames. Apart from the differences in velocity, other static flow parameters remain the same.

The ZND solution is derived in the shock stationary reference frame from the reactive Euler equations. It assumes a one dimensional flow and treats the shock as a nonreactive discontinuity that triggers a region of heat addition due to chemical reaction, after which a steady CJ detonation is established. It relates heat addition to flow properites by solving the Rankine-Hugoniot and Rayleigh equations to determine the pressure and specific volume

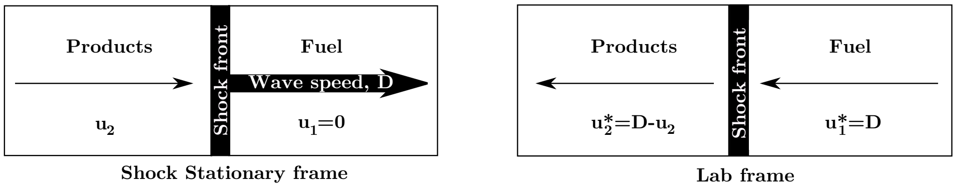

Figure 3.1 Sketch of the flow properties ahead and behind a detonation wave in the shock stationary reference frame (left) and lab reference frame (right).

equations as a function of heat of reaction, q, scaled by the reactant mass fraction, Y. The heat of reaction is given by

$$q = \frac{1}{2}\frac{(M_1^2-1)^2}{(\gamma^2-1)M_1^2} \tag{3.1}$$

for some assumed approach Mach number M_1. If an approaching Mach number is known or assumed, the pressure

$$p = p_1\frac{1+\gamma M_1^2 \mp \gamma\sqrt{(M_1^2-1)^2-2(\gamma+1)(\gamma-1)M_1^2 q(1-Y)}}{\gamma+1} \tag{3.2}$$

and specific volume

$$v = v_1\frac{1+\gamma M_1^2 \pm \sqrt{(M_1^2-1)^2-2(\gamma+1)(\gamma-1)M_1^2 q(1-Y)}}{(\gamma+1)M_1^2} \tag{3.3}$$

are expressed solely as functions of reactant mass fraction Y. The interchangeable sign in these equations correspond to strong (addition) and weak (subtraction) detonations affiliated with the upper CJ point, seen in Fig. 1.2.1. The temperature is found simply by using the nondimensionalized equation of state

$$p = \rho T. \tag{3.4}$$

Therefore, the entire thermodynamic state of the flow at any point in the domain can be expressed as a function of the reactant mass fraction. This is arbitrary for any given reaction behavior.

The limiting cases $Y = 0$ and $Y = 1$ are located at the outer edges of the reaction zone and correspond to the CJ state and the post shock state respectively. At the post shock state, no fuel has been used ($Y = 1$) and no heat has been added to the flow. Conversely, at the CJ state, all fuel has been consumed ($Y = 0$), the chemical reaction is complete, and all chemical heat has been added to the flow. The flow variables (p, ρ, T) may be calculated for these limiting cases using equations 3.2 and 3.3. Furthermore, when $Y = 1$ equations 3.2 and 3.3 reduce to the Rankine-Hugoniot shock jump relations[53]. The post shock Mach number, pressure, and density are given by

$$M_s = \sqrt{\frac{1+\frac{\gamma-1}{2}M_1^2}{\gamma M_1^2-\frac{\gamma-1}{2}}}, \tag{3.5}$$

$$p_s = p_1 \left(\frac{1 + \gamma M_1^2}{1 + \gamma M_s^2} \right), \tag{3.6}$$

and

$$\rho_s = \rho_1 \left(\frac{1 + \gamma M_s^2}{1 + \gamma M_1^2} \right) \left(\frac{M_1}{M_s} \right) \tag{3.7}$$

where the subscript s denotes post shock value. The temperature is found with the equation of state. Equations 3.5-3.7 are equivalent to Eq. 3.2 and 3.3 at the post-shock state $Y = 1$.

To find the distribution of thermodynamic states in between the CJ and post shock states, some finite reaction model must be included. The reaction rate $\dot{W}$ is the rate of consumption of the reactant mass fraction Y. A simple one-step Arrhenius expression is specified to describe $\dot{W}$. Originally described as a function of time, Eq. 2.8 can be easily rearranged to be a function of space. First, the chain rule is applied to attain a differentiation with respect to the spacial coordinate x. Then dx/dt is expressed as the velocity u, giving

$$\frac{dY}{dt} = \frac{dY}{dx}\frac{dx}{dt} = \frac{dY}{dx}u. \tag{3.8}$$

This allows dY/dx to be expressed as

$$\frac{dY}{dx} = \frac{1}{u}\left[B\rho Y e^{-E_a/T} \right], \tag{3.9}$$

This ODE can be solved to provide the spatial distribution for fuel mass fraction, $Y(x)$, downstream of the shock discontinuity. With $Y(x)$ known, Eq. 3.2-3.4 provide the thermodynamic state in the reaction zone.

3.2 1-D Hot Spot Models

This work presents two implementations of a model hot spot. First, a simplified version with just a plateau region is examined to demonstrate the thermomechanical response of the surrounding mixture to the hot spot reaction. The second implementation combines a plateau with a temperature gradient and demonstrates the effect of the plateau region on the temperature gradient.

A stoichiometric mixture of Hydrogen-Air is modeled using a one-step Arrhenius reaction rate with parameters given in Table 3.1 with respect to a reference thermodynamic state.

Parameter	Value
P_o	1 atm
T_o	300 K
γ	1.4
R	398 J/(kg K)
a_o	347 m/s
B	2.26E+9 (1/s)
E_a	33 γRT_o
q	12 γRT_o

Table 3.1 Arrhenius reaction rate parameters [1] presented in terms of the given reference state (subscript o).

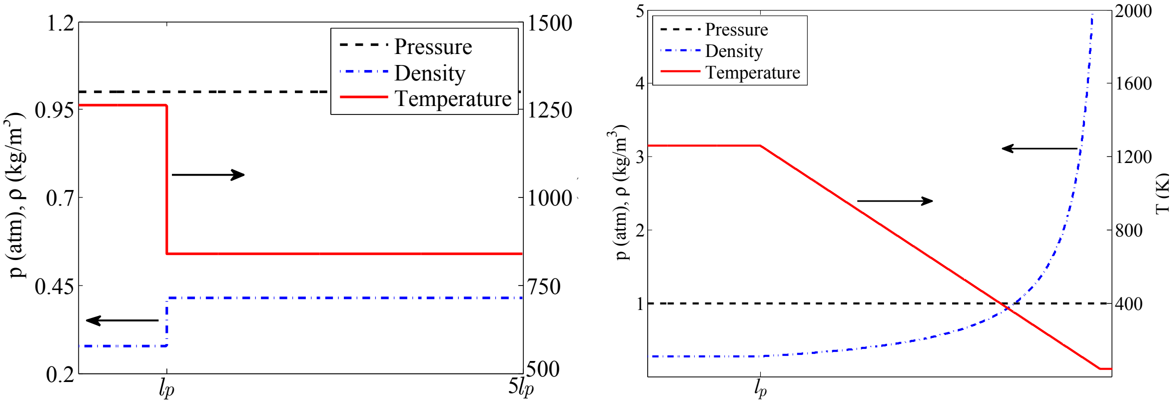

(a) Plateau only model

(b) Plateau with gradient model

Figure 3.2 Initial conditions for hot spot models.

Here, R is the universal gas constant, calculated for the weighted average of a stoichiometric H_2-Air reactive mixture. The dimensional length scale l' is chosen as one millimeter so that the dominant nondimensional length scale associated with the hot spot behavior is $O(1)$.

3.2.1 Plateau Only Model

The first hot spot model in this work consists of a plateau region at a higher temperature than its surroundings. This corresponds to the limiting case of $\Delta \rightarrow 0$, or no linear gradient portion. The initial conditions inside the hot spot plateau region are $T_p = 1260$ K, $p_p = 1$ atm, and $\rho_p = 0.24$ kg/m^3. The subscript p denotes plateau conditions. The ambient conditions are $T_a = 840$ K, $p_a = 1$ atm, and $\rho_a = 0.36$ kg/m^3. These conditions are shown in Fig. 3.2(a) for a hot spot of arbitrary plateau length, l_p.

Three timescale ratios are chosen as $\tau_e/t_a = 10, 1$ and 0.1 to represent the various fluid responses. A convention for τ_e must be chosen to define l_p, because the actual excitation time will vary based on the type of reaction, *e.g.*, isochoric (τ_e^v), isobaric (τ_e^p), or somewhere inbetween. Since the focus of this work is on compressibility effects, effects typically associated with inertial confinement, the acoustic timescale ratio τ_e/t_a will be constructed using the isochoric excitation time, τ_e^v. Based on this convention, the excitation time, τ_e, can be assumed henceforth to be the isochoric excitation time, τ_e^v, unless specified otherwise. Using the initial hot spot temperature $T_p = 1260$ K, the isochoric excitation time is calculated as $\tau_e = \tau_e^v = 0.4$ μs, giving a reaction lengthscale of $L = 0.34$ mm. The chosen timescale ratios can then be used to find the plateau lengths $l_p = L/10, L$, and $10L$. A domain size of $5l_p$ is prescribed for each case.

3.2.2 Plateau with Gradient Model

The second hot spot model used in this work consists of a plateau region combined with a linear temperature gradient. This approach is used to model the effects of a rounded peak in temperature on the surrounding region with a more substantial temperature gradient. The conditions inside the plateau are the same as those in the plateau only model. This plateau is then surrounded by a temperature gradient. Pressure is constant throughout the domain. The density is determined using the equation of state. These initial conditions are shown in Fig. 3.2(b).

Four different cases will be closely examined with this model. First, a case is run with no plateau to characterize the behavior with only a temperature gradient. The slope of the temperature gradient creates a reaction that is close to establishing a detonation independent of a plateau region, but just weak enough that the reaction does not couple with the shock wave. It should be noted that the critical gradient length used in this work, from one-step kinetics, will likely be 2-3 orders of magnitude smaller than the length computed using detailed kinetics [41]. The remaining three cases will combine this gradient with the plateau lengths $l_p = L/10$, L, and $10L$, corresponding to timescale ratios $\tau_e/t_a = 10, 1$, and 0.1 respectively.

Finally, temperature gradients with different slopes are examined. This results in a two parameter study described by the plateau length, l_p and the gradient slope. In this work the slope, S, is controlled by the length of the gradient region, l_g. This gradient length is defined as $l_g = (T_i - T_a)/S$. As the gradient length becomes larger, the slope decreases. Cases are run throughout a broad parameter space that fully characterizes the range of behaviors from this interaction.

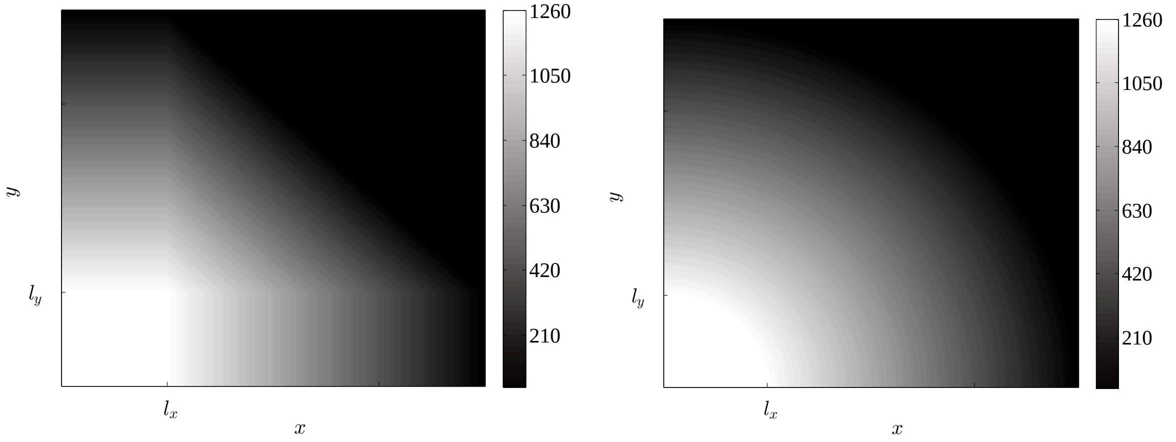

(a) Rectangular hot spot model (b) Elliptical hot spot model

Figure 3.3 Initial temperature distribution for hot spot models.

3.3 2-D Hot Spot Models

Two 2-D hot spot models, rectangular and elliptical, are used to extend the analysis performed in the 1-D study. Both models are used to explore symmetric and asymmetric hot spots. Hot spots with symmetric plateaus will be considered to show how multiple dimensions affect the hot spot characterization. Asymmetric plateaus will be examined to explore effects of asymmetry and non-unity hot spot aspect ratio.

The two hot spot models are composed of a constant temperature plateau region surrounded by a linear temperature gradient. This approach models the effect of a rounded peak in temperature on the surrounding region with a more substantial temperature gradient. First, a rectangular plateau with height l_y and width l_x will serve as a direct comparison to 1-D simulations. The second model features an elliptical plateau as a more realistic hot spot model. This model accounts for curvature effects present in real systems.

Similar to the 1-D problem, a stoichiometric Hydrogen-Air mixture is modeled using a one-step Arrhenius reaction rate (parameters given in Table 3.1). The initial temperature distributions along the x- and y-axes are equivalent to the 1-D initial condition, where the temperature gradient was chosen such that it is slightly too steep to form a detonation without any plateau region in 1-D. The initial temperature distribution can be seen for both models in Fig. 3.3. For all cases, the initial conditions within the plateau region are $T_p = 1260$ K, $p_p = 1$ atm, and

$\rho_p = 0.24$ kg/m^3. The subscript p denotes plateau conditions. Initially, pressure is constant throughout the domain and the plateau is surrounded by a linearly decreasing temperature gradient. The isochoric excitation time is calculated as $\tau_e = \tau_e^v = 0.4$ μs, giving $L = 0.34$ mm for the initial hot spot conditions. The gradient length is defined as $l_g = (T_a - T_p)/S = 30L$, where T_a is the temperature of the surroundings and the gradient slope is $S = -119$ K/mm.

To establish a baseline behavior for the temperature gradient in 2-D, a case without a plateau region, $l_x = l_y = 0$, will be run. Multidimensional effects are explored using symmetric plateau regions with equal side lengths, $l_x = l_y = l$. Three different cases are used with each model, letting $l = L/10, L$, and $10L$ which correspond to timescale ratios $\tau_e/t_a = 10, 1$, and 0.1, respectively. The plateau reaction generates a compression wave directed away from the plateau and an expansion wave directed towards the plateau center.

In general, hot spots are not usually symmetric. Sankaran and colleagues [23, 25, 24] focus on initial temperature fields with asymmetric hot spots. To study the effects of this aspect ratio, additional cases will be run with both models letting $l_y > l_x$. The lengths l_y and l_x correspond, respectively, to the height and width of the rectangular plateau and the semi-major and semi-minor axes of the elliptical plateau. This results in two different acoustic timescales for an asymmetric plateau region. On the horizontal axis the acoustic timescale is defined as $t_a^x = l_x/a$. Similarly, the vertical direction has an acoustic timescale, $t_a^y = l_y/a$.

The three aspect ratios examined are $t_a^y/t_a^x = l_y/l_x = 2, 5$, and 10. To study this effect, a partially confined plateau ($\tau_e = t_a^x$) has been selected as the fixed acoustic timescale ratio along the x-axis. An unconfined plateau along the x-axis ($\tau_e \gg t_a^x$) would allow rapid fluid expansion in the x-direction to occur during the reaction timescale, making additional expansion due to multidimensional effects difficult to isolate. On the other hand, having a confined plateau ($\tau_e \ll t_a^x$) in the x-direction readily reproduces limiting 1-D behavior. Therefore, the chosen acoustic timescale ratio along the x-axis, $\tau_e/t_a^x = 1$, is the most pertinent to examine. As the aspect ratio t_a^y/t_a^x increases, behavior along the x-axis is expected to approach the 1-D model behavior.

CHAPTER 4. NUMERICAL METHODS

The main focus of this thesis is to demonstrate the physical phenomena of hot spots and to show they can be characterized by the acoustic timescale ratio. To this end, certain numerical techniques are implemented to solve the set of partial differential equations governing this type of flow. This chapter will be a concise overview of the methods employed.

The dynamically Adaptive Wavelet-Collocation Method (AWCM) is used to perform all calculations in this study [54, 55]. A revised hyperbolic solver [56] developed for the AWCM is used to solve the reactive Euler equations. These methods have been developed and tested thoroughly by our group and colleagues and are the subject of many studies [56, 34, 35, 57].

4.1 Adaptive Wavelet Collocation Method

The AWCM was developed specifically for solving problems with a wide range of spatial and temporal scales [54]. The work presented in this thesis has very localized structures that need high resolution to resolve. It would be impractical to use a uniform grid to solve such problems, since any smooth areas do not require the same level of resolution. The AWCM takes advantage of the fact that wavelet methods are very effective at compressing these types of sharp transitions in the solution. It dynamically adapts the grid to properly resolve these localized structures, while keeping a reduced amount of points in areas that are smooth.

The AWCM is based on wavelet decomposition [58, 59], which represents any function $u(\boldsymbol{x})$ in an n-dimensional space by using basis functions, or wavelets $\psi_{\boldsymbol{\ell}}^{\mu,j}(\boldsymbol{x})$, as

$$u(\boldsymbol{x}) = \sum_{\boldsymbol{k}\in\mathcal{K}^0} c_{\boldsymbol{k}}^0 \phi_{\boldsymbol{k}}^0(\boldsymbol{x}) + \sum_{j=0}^{+\infty} \sum_{\mu=1}^{2^n-1} \sum_{\boldsymbol{\ell}\in\mathcal{L}^{\mu,j}} d_{\boldsymbol{\ell}}^{\mu,j} \psi_{\boldsymbol{\ell}}^{\mu,j}(\boldsymbol{x}). \tag{4.1}$$

Here, $c_{\boldsymbol{k}}^0$ and $\phi_{\boldsymbol{k}}^0(\boldsymbol{x})$ are scaling functions on the lowest level of resolution, $d_{\boldsymbol{\ell}}^{\mu,j}$ are the wavelet coefficients, k and ℓ denote index in n-dimensional space, and $\mathcal{K}^0$ and $\mathcal{L}^{\mu,j}$ are n-dimensional index sets associated with scaling functions at zero level of resolution and wavelets of family μ and j level, respectively.

With this method, every point is associated with a wavelet. [54] This allows the grid to be adapted corresponding to wavelets with coefficients greater than a certain threshold parameter, ϵ. The level of resolution doubles the number of available points with each increase. However, of these available points, only those needed to resolve the solution to the level of accuracy prescribed by ϵ are used.

The reactive Euler equations are hyperbolic in nature, which naturally form discontinuities, *i*.e. shock waves. An infinite level of resolution is required to resolve this type of discontinuity, which is not attainable. It is reasonable to limit the maximum level of resolution, $j_{\max}$, to avoid exceeding computational resources. This allows for refinement to a prescribed level of resolution.

4.2 Hyperbolic Solver

A hyperbolic solver is used in conjunction with the AWCM to solve the problems presented in this thesis. Nonlinear partial differential equations (PDEs) such as the reactive Euler equations can develop discontinuities within the solution due to their hyperbolic mathematical nature. Additional treatment is required in areas with these discontinuities. A flux limiter function is used to apply numerical viscosity in discontinuous locations.

Van Leer flux limiting is used to minimize numerical diffusion while maintaining nonlinear stability [60, 61]. To present the numerical scheme used for spatial discretization, consider the scalar conservation equation with an additional term for the artificial viscosity represented as

$$\frac{\partial u}{\partial t} + \frac{\partial f}{\partial x} = \frac{\partial}{\partial x}\left(\nu\left(\Phi\right)\frac{\partial u}{\partial x}\right). \tag{4.2}$$

where ν is the artificial viscosity which is a function of the limiter function, Φ. The discretized equation using a second-order central differencing scheme with artificial diffusive terms is

$$\frac{\partial u_i}{\partial t} = \frac{f_{i+1} - f_{i-1}}{2\Delta x} + \frac{\nu_{i+1/2}\frac{u_{i+1}-u_i}{\Delta x} - \nu_{i-1/2}\frac{u_i - u_{i-1}}{\Delta x}}{\Delta x} \tag{4.3}$$

where

$$\nu_i = \frac{1}{2}\Phi_i\left(a_i + |u_i|\right)\Delta x \tag{4.4}$$

The limiter function is a normalized function of wavelet coefficient that is zero in smooth regions and increases to a maximum of one near contact discontinuities. This applies numerical viscosity only near discontinuities and has no effect on the velocity coefficient elsewhere.

The third-order total variation diminishing (TVD) Runge-Kutta scheme used for time integration [62] can be written as

$$\begin{aligned} u^{*} &= u^{n} + \Delta t L\left(u^{n}\right), \\ u^{**} &= \tfrac{3}{4}u^{n} + \tfrac{1}{4}u^{*} + \tfrac{\Delta t}{4}L\left(u^{*}\right), \\ u^{n+1} &= \tfrac{1}{3}u^{n} + \tfrac{2}{3}u^{**} + \tfrac{2\Delta t}{3}L\left(u^{**}\right), \end{aligned} \tag{4.5}$$

where the spatial derivative $L(u) = f(u)_x$ is approximated by a TVD finite difference. The TVD-RK3 scheme is great for the purpose of this work because it was developed using fluxes rather than cell-averages which causes it to be essentially non-oscillatory near discontinuities.

4.3 Verification with ZND Solution

To demonstrate the accuracy of the methods used for the work presented in this thesis, simulations will be run and compared with the ZND solution. The structure of a detonation using the ZND model is well known, making it a good candidate when comparing results. First the analytical solution is presented, followed by the comparison with numerical results from the AWCM hyperbolic solver. This model will also be used to discuss the importance of grid resolution in detonation simulations.

4.3.1 Analytical Solution

A ZND detonation is set up assuming the detonation wave is traveling at $M_1 = 5$. The non-dimensional heat of reaction $q = 12$ is found using Eq. 3.1. A non-dimensional activation energy of $E_a = 10$ and pre-exponential factor $B = 5$ are used to simulate the reactive mixture. After defining the undisturbed state, the post shock and CJ states in the shock attached reference frame are calculated with Eq. 3.2-3.4 and all values are listed in Table 2. To calculate the fuel distribution downstream of the shock, the reactant mass fraction is obtained by solving Eq. 3.9 using a fourth order Runge-Kutta scheme. The ZND solution is solved in the domain x ∈ [0,

Variable name	Initial Condition	Post Shock	CJ State
u - Velocity	5	1	3
p - Pressure	$1/\gamma$	20.71	10.71
ρ - Density	1	5	1.67

Table 4.1 Initial, Post shock, and CJ state values in the shock attached reference frame.

20]. Initially Y is set to one and it decays to zero as it approaches the end of the reaction zone. Assuming a strong detonation, the thermodynamic distribution is found using Eq. 3.2 - 3.4 with the values of reactant mass fraction obtained downstream of the shock. The undisturbed fluid state is appended to the solution to show the upstream state and the entire solution is translated to simulate $t = 7$ when the shock front is located at $x = 20$.

A detonation wave may be looked at from two different perspectives: the lab reference frame, where the shock is moving, or the shock frame, where the shock is stationary with flow traveling through it. Since the two solutions are in different reference frames, a conversion between the two frames must be established. From mass conservation

$$\rho u = \text{const.} \tag{4.6}$$

The velocity field in the shock reference frame is found using mass conservation with respect to the unburnt state

$$u^* = \frac{\rho_1 u_1^*}{\rho}. \tag{4.7}$$

The theoretical wave speed

$$D = M_1 \sqrt{\gamma p_1 v_1} \tag{4.8}$$

is used to convert the velocity field in the shock reference frame to the velocity field in the lab reference frame

$$u = D - u^*. \tag{4.9}$$

With the incoming flow $M_o = 5$, the wave speed is determined using Eq. 4.8 to be $D = 5$. The CJ velocity in the shock reference frame is calculated to be $u^*_{CJ} = 3$, using Eq. 4.7 and the density values from table 2 . Converting from the shock reference frame to the lab reference

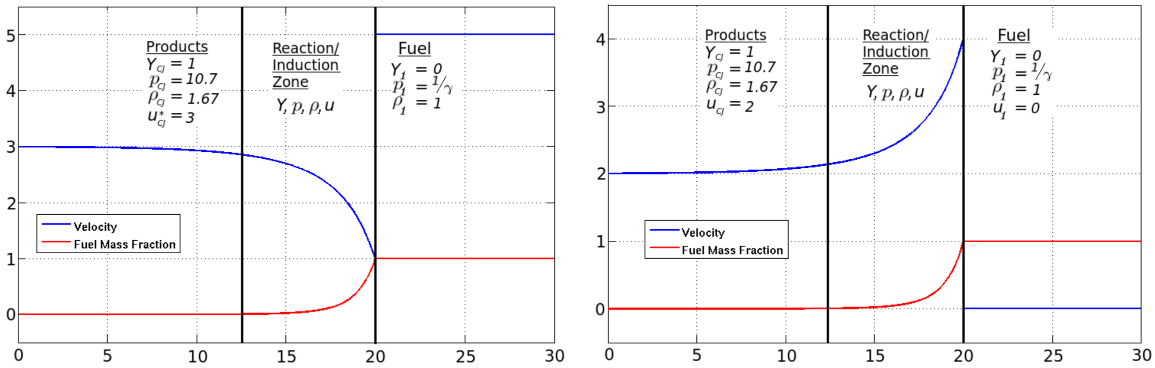

(a) Shock stationary reference frame

(b) Lab reference frame

Figure 4.1 Comparison of detonation in (a) shock stationary and (b) lab (shock moving) reference frames.

frame using Eq. 4.9 gives $u_{CJ} = 2$. The differences in the velocity field between the shock frame and lab frame can be seen in Fig. 4.1(a) and 4.1(b).

4.3.2 Euler Solution

As discussed in the previous two chapters, molecular diffusion, thermal conduction, and viscous effects can be ignored. In the absence of transport effects the Navier-Stokes equations reduce to the Euler equations. The flow can be modeled using the reactive Euler equaitons where an additional transport equation is solved for the fuel density.

The initial condition for the hyperbolic solver is a CJ wave. Therefore, it takes time for the solution to become steady and evolve to a ZND detonation. Figure 4.2 shows the progression of the 1-D Euler solution from $t = 0$ to $t = 7$. For reference, the analytical solution has been plotted as a solid line at $t = 7$. The initial transient state for density has the most notable change between $t = 0$ and $t = 1$ as its post shock value increases to approximately 4. There is also a large jump in pressure just behind the shock. This state, just behind the shock is referred to as the von Neumann spike and shows the drastic difference between the CJ detonation model and the ZND model. It can be seen that the 1-D Euler solution is nearly steady at $t = 7$. However, the solution was allowed to propagate further to $t = 20$ due to small discrepancies that can be seen in the temperature, density, and velocity plots. This waviness eventually levels out, and will be discussed later in Section 4.3.3.

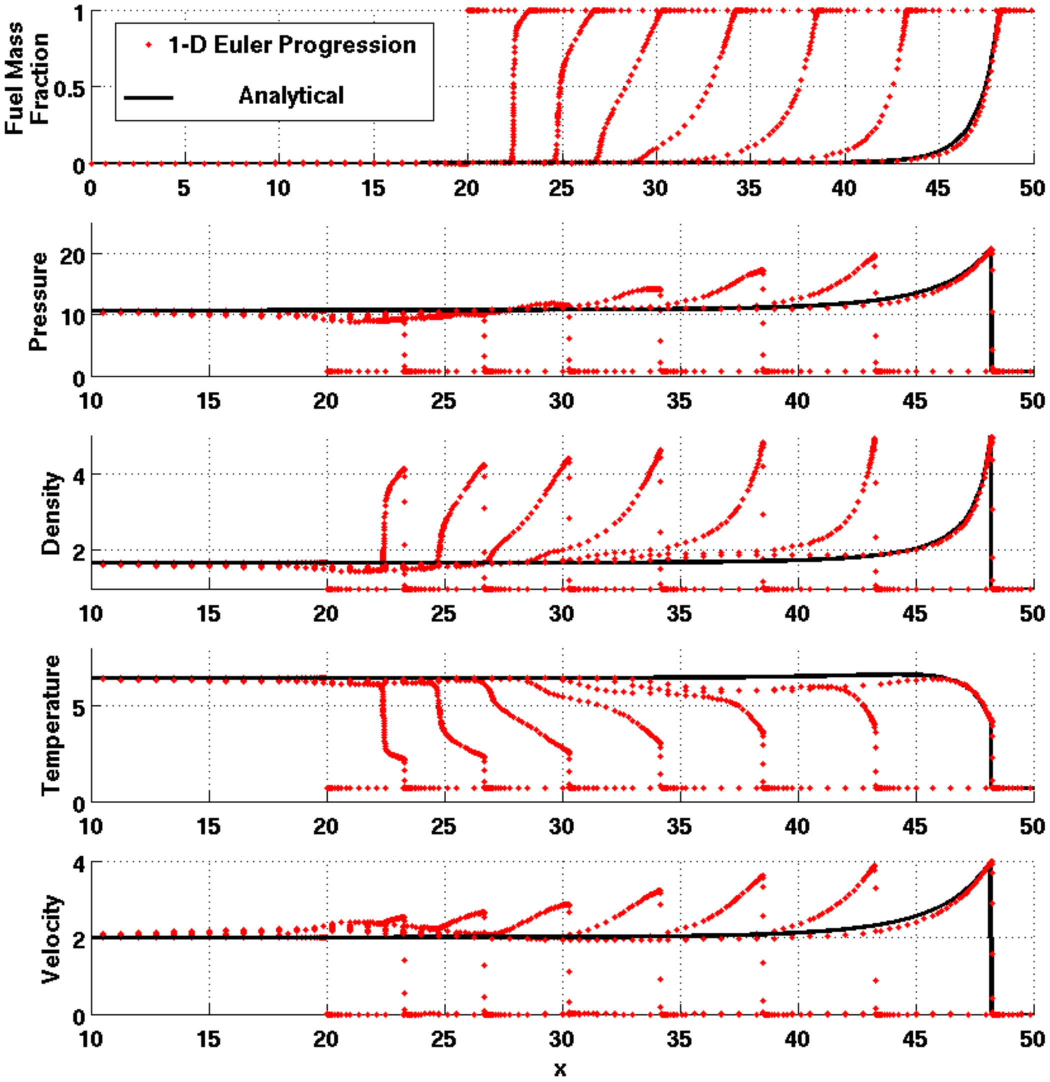

Figure 4.2 Progression of the 1-D Euler solution from $t = 0$ to $t = 7$

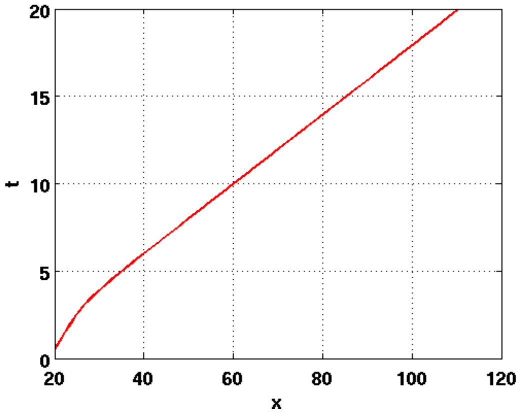

Figure 4.3 x-t diagram of reaction wave loctation.

To confirm that the detonation propagates at the correct speed, the detonation position is plotted as a function of time in Fig. 4.3. The inverse slope of this curve is the numerical detonation speed. Using a linear regression on the linear portion of the curve, the slope is found to be 0.199. This corresponds to a wave speed of 5.04, which matches the theoretical detonation speed $D = 5$ with an error of 0.8%.

4.3.3 Resolution Dependence

To demonstrate the effect of grid size on the resolution of the solution, a close up view of the density has been provided in Figure 4.4. In this case, density is diffused most heavily from the hyperbolic solver, thus density is the variable inspected to observe if the solution has been fully resolved. It is important to look at how many points are needed to resolve this spike. The portion from the shock until the fuel mass fraction reaches $Y = 0.5$ is called the half reaction length, $\Delta_{1/2}$, and will require a high density of grid points to resolve. The half reaction length according to the ZND model is $\Delta_{1/2} = 0.81$. The number of grid points per half reaction length for this simulation is found with $n_{1/2} = \Delta_{1/2}/\Delta x$. Figure 4.4(a) shows an under-resolved case with $n_{1/2} = 36$. It can be seen that at its highest point the numerical solution approaches 4.46, which is approximately 89% of the theoretical value. In Figure 4.4(b), the solution for density approaches 4.96, or 99% of the theoretical value. The case on the right is considered to be fully resolved and has 222 points to resolve this half reaction length. This is consistent with the literature on how fine a grid must be to fully resolve a detonation wave [34].

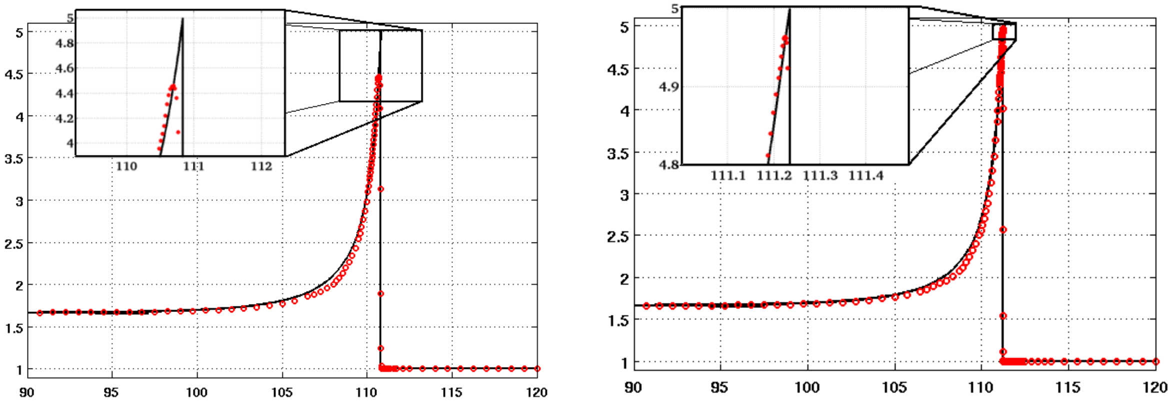

(a) $n_x = 36$

(b) $n_x = 222$

Figure 4.4 Close up view of density at $t = 20$ comparing the analytical and numerical solutions for density.

The numerical solution for both the 1-D Euler and ZND solutions are shown in Fig. 4.5 at time $t = 20$. The Euler solution in Fig. 4.5 is resolved with $n_{1/2} = 222$. At this point the detonation has propagated from $x = 20$ to $x \approx 111$. The analytical solution may simply be translated along x using the wave speed D and elapsed time t. Minor differences can be seen in the reaction zone; this could be due to not letting the reaction stabilize fully as the wave propagates. It could also be caused by the inherent instability encountered with the 1-D detonation waves [18]. Overall they match well. The wave speed determined form the 1-D Euler solution matches the theoretical speed ($D = 5$) to within 0.8%. It is also shown that the density at the von Neumann spike will reach 99% of the theoretical value, with proper resolution.

4.4 Resolution

A base grid of 40 points is used with 13 levels of refinement for the 1-D cases. The number of required refinement levels was determined by increasing the resolution until the peak pressure at the von Neumann spike changed by only 0.6% for the case with the largest domain. This results in a grid with $N = 163,840$ effective grid points, which is used for both the plateau only and the plateau with gradient cases. Since the same number of points is used for each case, the error in the pressure at the von Neumann spike will be less than 0.6% for the other cases.

In the 2-D cases, a base grid of 40×40 points is used with a maximum of nine refinement lev-

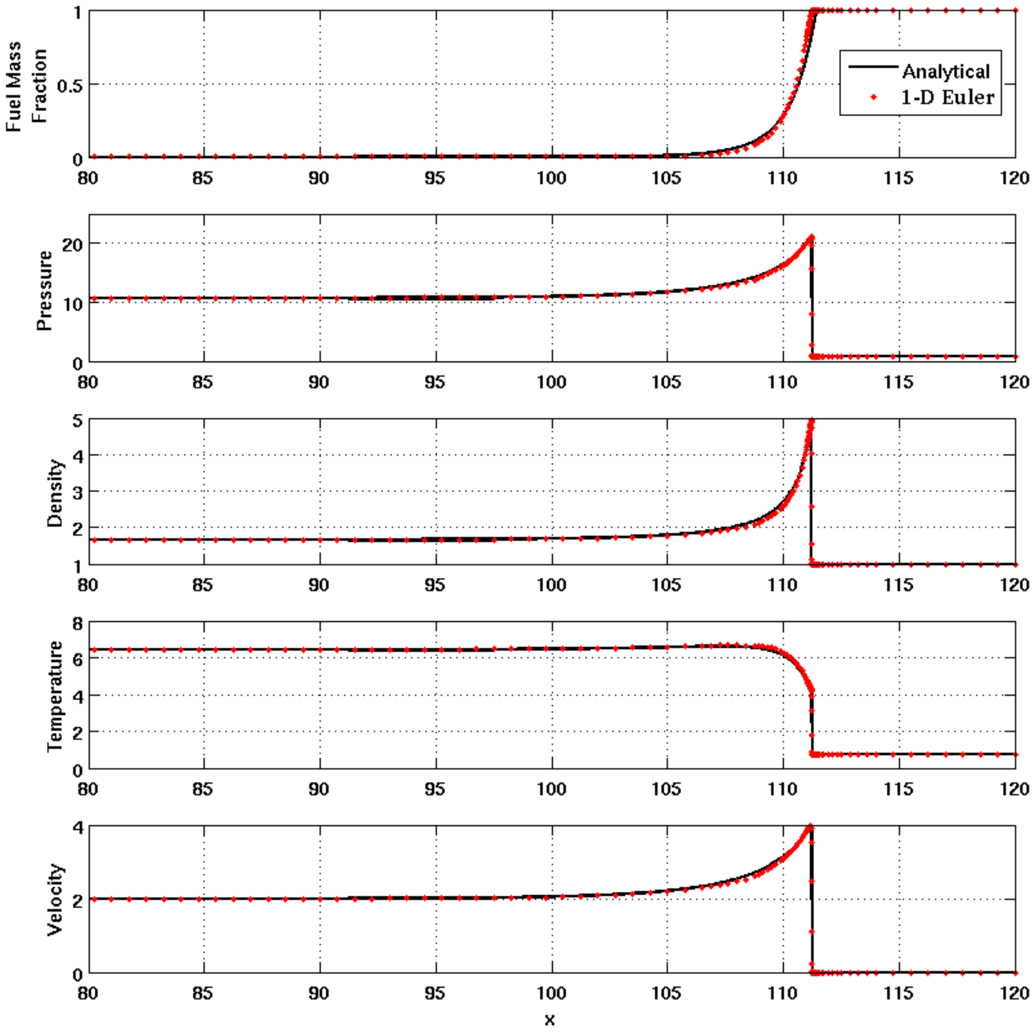

Figure 4.5 1-D Euler solution compared to the Analytical solution for the ZND model at $t = 20$

els. The number of required refinement levels was determined by increasing the resolution until the half reaction location changed by only 1% after t_a for the confined square case ($\tau_e \ll t_a$). This results in an effective grid with $N = 10,240 \times 10,240$ effective grid points, corresponding to a grid resolution of $\Delta x = 1.3\mu m$ at the finest level. Grid resolution is kept constant for all other 2-D cases.

4.5 Boundary Conditions

In the 2-D work presented within, detonations (if formed) are traveling in the positive x- and y-directions. In general the fluid ahead of the detonation is in a quiescent state. Since the simulation is terminated prior to the detonation's arrival at the right and top boundaries, conditions at these boundaries are relatively inconsequential. Left untreated, the initial temperature gradient will induce solution instability at these boundaries. Therefore, the right and top boundaries boundaries are treated with Neumann conditions given as

$$\left.\begin{matrix} \frac{\partial \rho}{\partial x} \\ \frac{\partial \rho u}{\partial x} \\ \frac{\partial \rho v}{\partial x} \\ \frac{\partial \rho e_T}{\partial x} \\ \frac{\partial \rho Y}{\partial x} \end{matrix}\right\} = 0 \quad \text{and} \quad \left.\begin{matrix} \frac{\partial \rho}{\partial y} \\ \frac{\partial \rho u}{\partial y} \\ \frac{\partial \rho v}{\partial y} \\ \frac{\partial \rho e_T}{\partial y} \\ \frac{\partial \rho Y}{\partial y} \end{matrix}\right\} = 0, \tag{4.10}$$

respectively.

The hot spots modeled in this work have been cut along a symmetry plane to reduce computational cost. The center of the hot spots is located at the origin, meaning the left and bottom boundaries are treated as symmetry boundaries, or adiabatic reflecting walls, given by

$$\left.\begin{matrix} \frac{\partial \rho}{\partial x} \\ \rho u \\ \frac{\partial \rho v}{\partial x} \\ \frac{\partial \rho e_T}{\partial x} \\ \frac{\partial \rho Y}{\partial x} \end{matrix}\right\} = 0 \quad \text{and} \quad \left.\begin{matrix} \frac{\partial \rho}{\partial y} \\ \frac{\partial \rho u}{\partial y} \\ \rho v \\ \frac{\partial \rho e_T}{\partial y} \\ \frac{\partial \rho Y}{\partial y} \end{matrix}\right\} = 0. \tag{4.11}$$

Here, all conserved variables have Neumann boundary conditions except x-momentum at the left wall and y-momentum at the bottom wall, which are treated with Dirichlet conditions. In

1-D simulations, boundary conditions at the left and right boundaries are identical to the 2-D conditions and the top and bottom conditions are inapplicable.

CHAPTER 5. RESULTS

First the hot spot problem will be examined with the 1-D model outlined in Section 3.2. Results are presented, analyzed, and discussed in Section 5.1. After this, Section 5.2 uses the methodology described in Section 3.3 to demonstrate how this 1-D model is extended to 2-D.

5.1 One Dimensional Results

The results from the plateau only cases will be presented first. Results from combining these plateaus with a single linear temperature gradient are presented in Sec. 5.1.2. Finally, additional temperature gradient slopes are explored and results for this two parameter study are presented in Sec. 5.1.3.

5.1.1 Plateau Only Model

For convenience, the case with $\tau_e/t_a = 10$ will be referred to as the “unconfined” case, $\tau_e/t_a = 1$ the “partially confined” case, and $\tau_e/t_a = 0.1$ the “confined” case. The average fuel fraction inside the plateau is plotted as a function of time for all cases in Fig. 5.1. The isochoric and isobaric fuel mass fractions are plotted for a homogeneous reactor as a reference. All cases fall between these two extremes. As expected, the unconfined case lies near the isobaric curve, the partially confined case lies between the two limiting curves, and the confined case lies on the isochoric curve. The isochoric and isobaric half-reaction times, τ_r^v and τ_r^p respectively, are labeled in the figure. The difference between the isochoric and isobaric half-reaction times is about 30%. There is a 58% difference between the isochoric and isobaric excitation times.

Figure 5.2 contains x-t contour plots for temperature and pressure for the unconfined, partially confined, and confined cases. The domain has been normalized by pocket length, l_p. The time axes have been shifted by the ignition delay times, τ_i^p and τ_i^v and normalized by

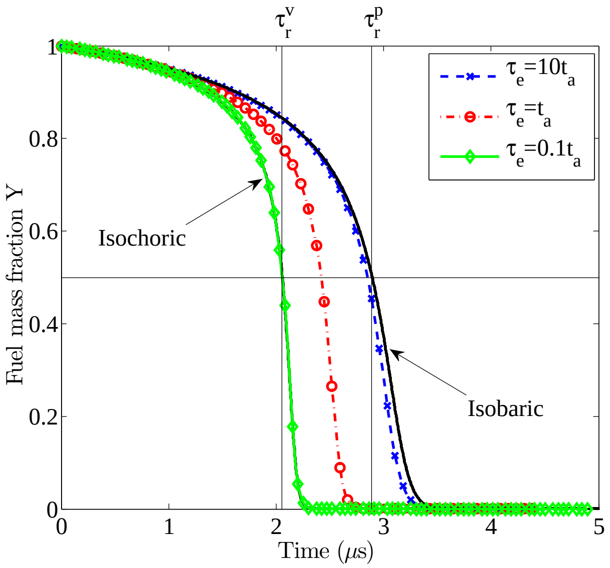

Figure 5.1 Fuel Mass fraction as a function of time for the three different cases are compared to the constant volume and constant pressure curves calculated using a spatially homogeneous reactor. The intersection of the horizontal and vertical black lines indicate the half-reaction times of the isochoric and isobaric cases, τ_r^v and τ_r^p, respectively.

excitation times, τ_e^p and τ_e^v. Thus, zero on the time axis corresponds to the end of the ignition delay period, and one corresponds to the end of the reaction. The isobaric ignition delay and excitation times, τ_i^p and τ_e^p, are used to shift and normalize the unconfined case while the isochoric ignition delay and excitation times, τ_i^v and $\tau_e = \tau_e^v$, are used for the other two cases. This translated format allows for a closer inspection of what is happening during the reaction and afterwards. Some figures have been extended to show times earlier than the ignition delay time since a small amount of fuel has been consumed by this point.

Two additional horizontal lines are shown, which correspond to the acoustic time, t_a, and excitation time, τ_e, with respect to zero. These are included on the unconfined and confined case plots to show the clear timescale delineation in these cases. An additional dashed line is superimposed on each plot to show the trajectory of a fluid element located at the edge of the plateau region.

The x-t diagram format used in this paper shows the temperature and pressure distributions throughout the entire domain, for all timesteps in the simulation. The contours display the thermomechanical response of the surroundings to the hot spot reaction. The reaction begins

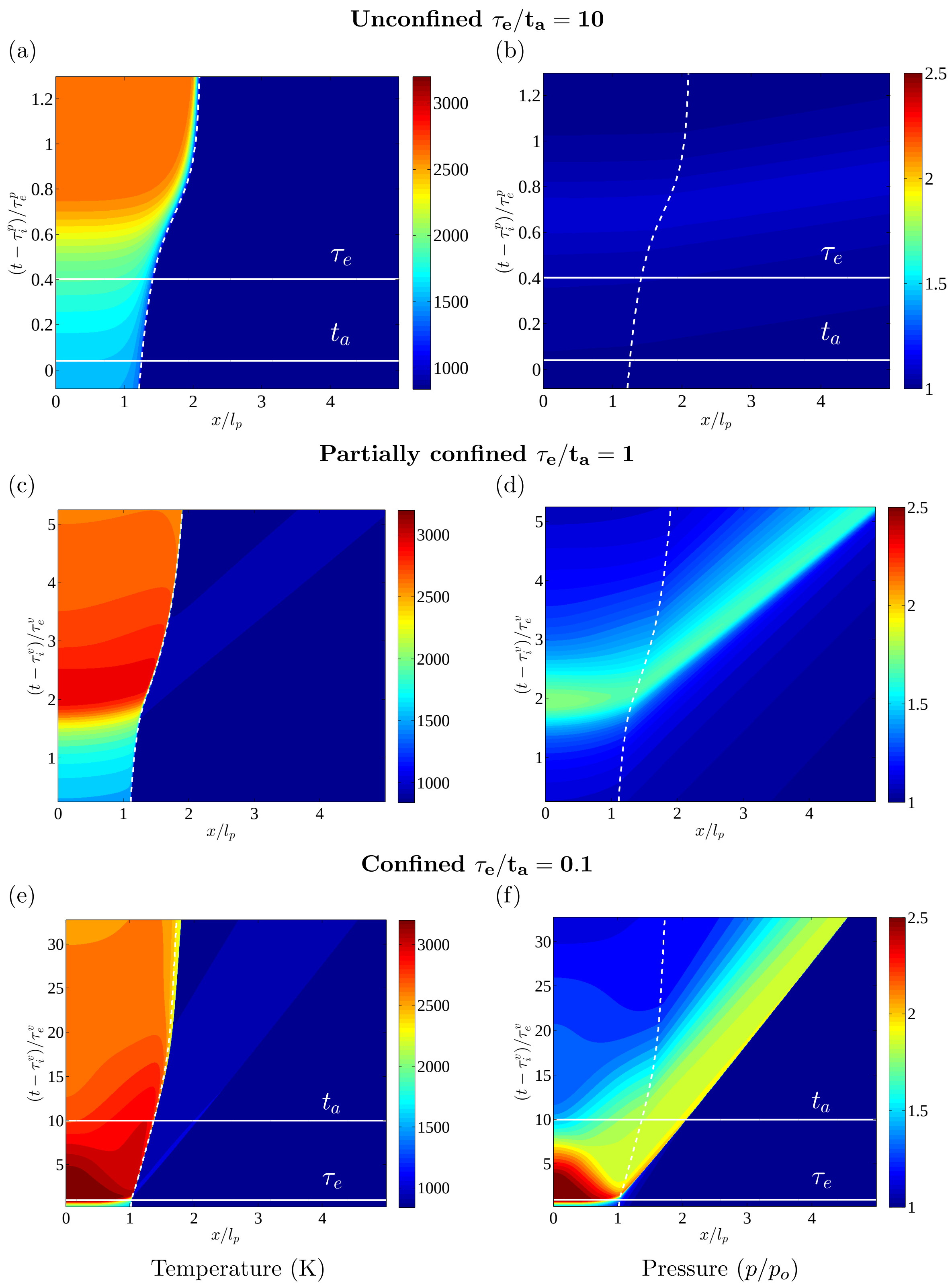

Figure 5.2 x-t diagrams of temperature and pressure for the plateau only cases.

at zero on the time axis after the ignition delay time has elapsed, $t - \tau_i = 0$. In general, the temperature and pressure within the hot spots increases as the reaction commences. Compression waves of different amplitudes can be observed in the pressure plots as disturbances that propagate in the $+x$ direction. As seen in Fig. 5.2 (f), shocks appear as discontinuous jumps in pressure.

Figures 5.2(a) and 5.2(b) show the results for the unconfined case. It can be seen that the acoustic timescale is an order of magnitude smaller than the excitation time. Figure 5.2(b) shows a small compression wave propagating through the domain as the chemical reaction occurs. This induces fluid motion, expanding the original hot spot edge to about twice its original size. The pressure increases by 9% during the reaction and is relatively uniform across the domain during the reaction period. The induced fluid motion and small pressure rise indicate the unconfined case reacts in a nearly constant pressure manner.

The results for the partially confined case are shown in Fig. 5.2(c) and 5.2(d). The excitation time for this case is equal to the acoustic timescale. The original hot spot size increases by about 15% during the reaction. Compression and expansion waves are generated simultaneously. The compression wave propagates in the positive x-direction and the expansion travels in the negative x-direction. The expansion wave reflects off the origin and follows behind the compression wave, resulting in a compression wave of finite width. The compression wave preheats the surrounding mixture a small amount for a short period (Fig. 5.2(c)). The hot spot length eventually grows to twice its original size. The compression wave generated in this case is about 30% stronger than in the unconfined case. The temperature rise in the hot spot is larger than in the unconfined case, reaching $T_{\max} \approx 2600K$ for the unconfined case and $T_{\max} \approx 3000K$ for the partially confined case.

The inertially confined case is shown in Fig. 5.2(e) and 5.2(f). For this case the excitation time is an order of magnitude shorter than the acoustic time, $\tau_e = t_a/10$, as indicated by the difference in magnitude of the horizontal lines. In this case the hot spot volume is not allowed to respond on the excitation timescale. This causes a shock wave to be transmitted through the domain as the reaction begins. This shock preheats the fluid, similar to the partially confined case, that can be seen in Fig. 5.2(e). The post-shock temperature is very similar to the peak

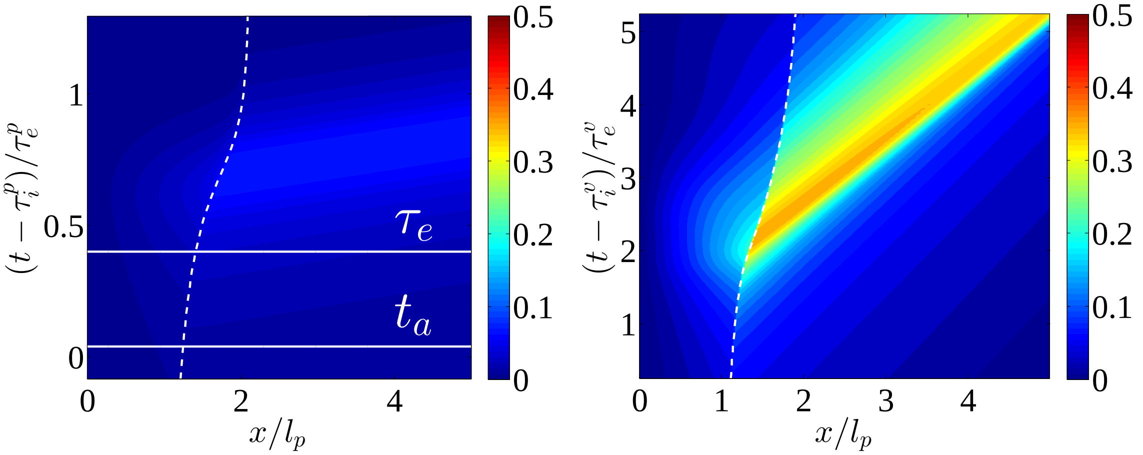

(a) Unconfined: $\tau_e/t_a = 10$

(b) Partially confined: $\tau_e/t_a = 1$

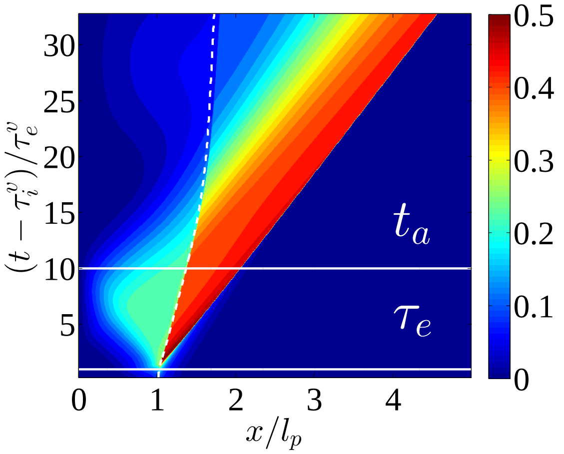

(c) Confined: $\tau_e/t_a = 0.1$

Figure 5.3 x-t diagrams of Mach number for each plateau only model case.

temperature of the compression wave in the partially confined case, with an average value of 1000 K. The pressure rises inside the hot spot by a factor of 2.5 over the initial pressure. This is notably higher than the ratio of the partially confined pressure rise of 1.5. The expansion wave reflects off the wall and follows behind the shock wave, reducing the pressure and temperature. The post shock pressure decreases with time as the expansion fan approaches the lead shock and reduces the fluid velocity.

Figure 5.3 shows x-t contours of the local Mach number. From left to right these represent the unconfined, partially confined, and confined cases. The induced Mach number for the unconfined case is almost negligible with respect to the other two cases and the fluid motion is induced throughout the reaction ($(t-\tau_i^p)/\tau_e^p < 1$). Alternatively, the majority of the fluid

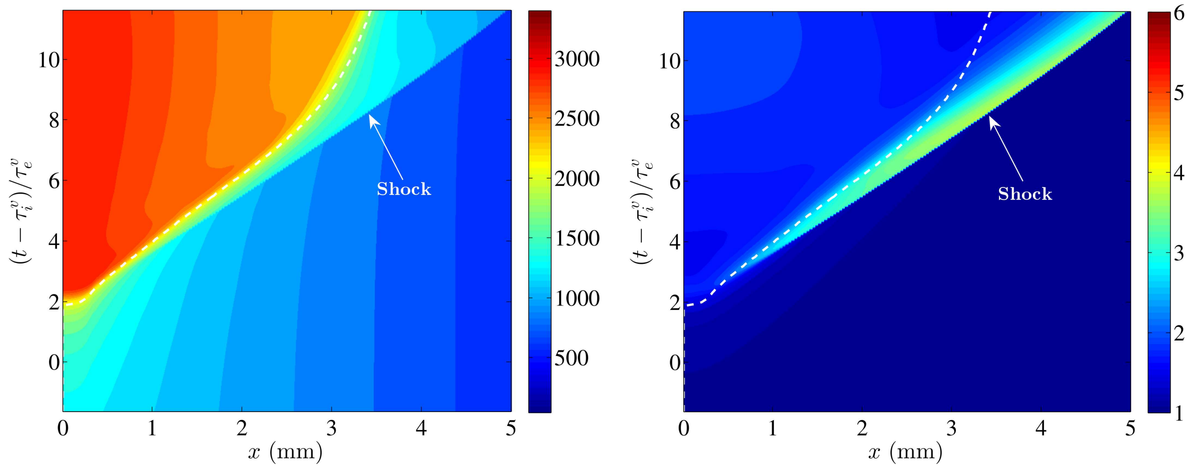

(a) Temperature (K)

(b) Pressure (p/p$_o$)

Figure 5.4 x-t diagrams of (a) temperature and (b) pressure for the gradient only ($l_p = 0$) case.

motion in the confined case is induced after the reaction in the plateau is finished ($(t-\tau_i^v)/\tau_e^v > 1$). As expected, the partially confined case induces substantial fluid motion after the reaction is finished in addition to throughout the reaction duration. However, a larger portion of the induced fluid motion happens post reaction. This behavior, *i.e.*, increasing Mach number with decreasing τ_e/t_a, is predicted by the asymptotic analysis performed by Kassoy [48, 49]

These results suggest that a plateau region can have either substantial or negligible impact on the behavior of a surrounding temperature gradient. The minimal pressure rise in the unconfined case implies it will have minimal impact upon any such gradient. Whereas, the partially confined and confined cases create mechanisms that may alter the temperature gradient in the surrounding reactive mixture.

5.1.2 Plateau with Gradient Model

The plateau only cases are combined with a temperature gradient of length $l_g = 30L$. Additionally, a case containing a temperature gradient and no plateau is simulated for reference and will be referred to as the "gradient only" case. Similar to the plateau only model, the case with $\tau_e/t_a = 10$ will be referred to as the "unconfined" case, $\tau_e/t_a = 1$ the "partially confined" case, and $\tau_e/t_a = 0.1$ the "confined" case.

Figures 5.4 and 5.5 show x-t diagrams for the four different cases. The time domain is

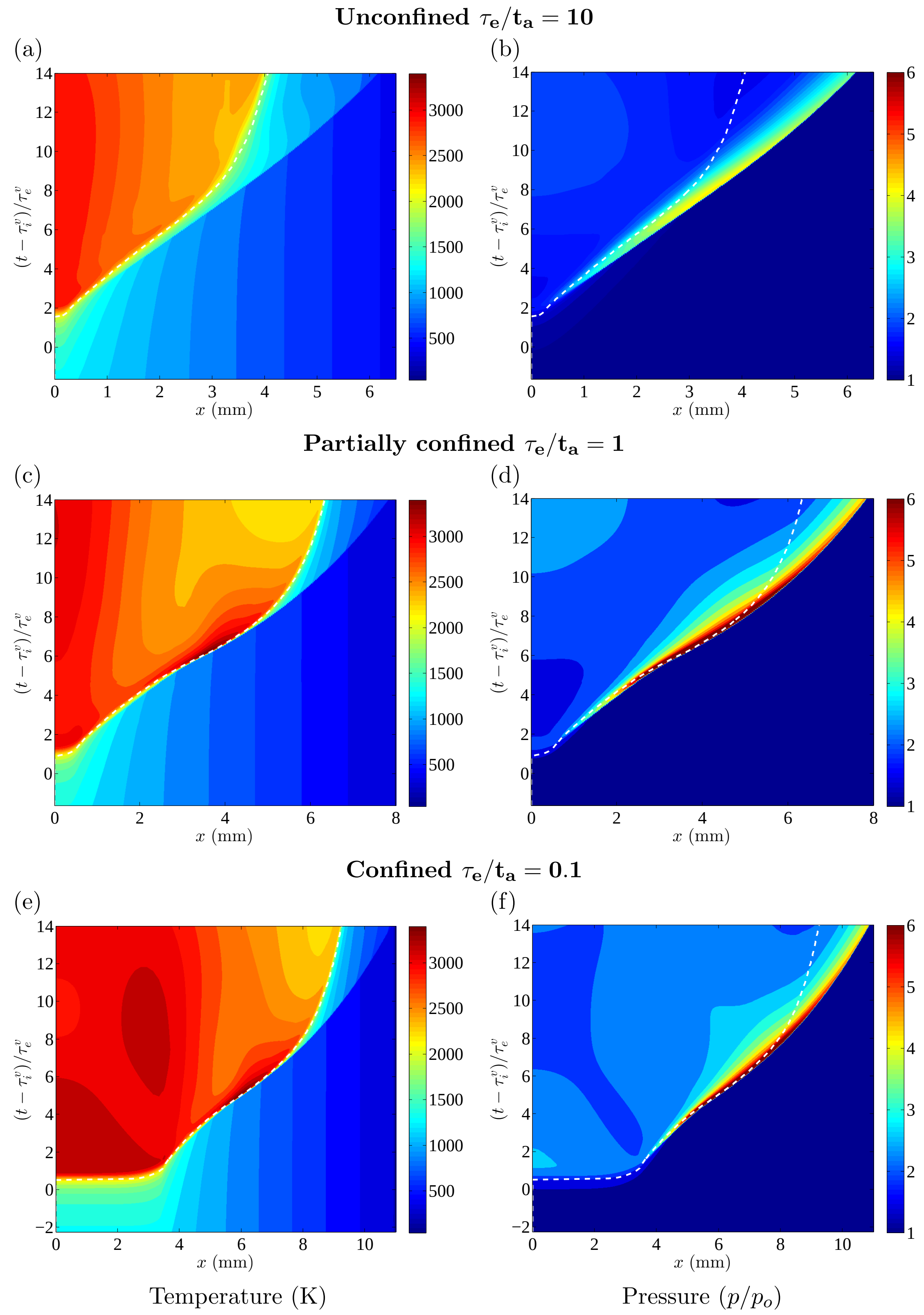

Figure 5.5 x-t diagrams of temperature and pressure for the gradient with plateau cases.

normalized identically to the plateau only cases, but the position x is no longer normalized by l_p in order to better compare results between cases. The figures have again been extended to show times earlier than the ignition delay time since a small amount of fuel has been consumed by this point. An additional dashed line is superimposed on each plot to show the location of half-reaction, which indicates the interface between the burnt and unburnt gases.

In the gradient only case a shock wave is formed and propagates through the domain as the chemical reaction occurs. As indicated by the dashed curves in Fig. 5.4, the reaction front is decoupled from the shock and decelerates with time. In addition, the initial temperature decreases as the reaction propagates further into the domain, causing the reaction to decelerate more quickly. Eventually the initial temperature becomes too low and the reaction is extinguished.

Figure 5.5 shows x-t diagrams of temperature and pressure for each plateau coupled with a temperature gradient case. Results for the unconfined case are shown in Fig. 5.5(a) and 5.5(b). For this case, a plateau with a timescale ratio $\tau_e/t_a = 10$ has been added to the gradient region. As anticipated, this type of plateau has little effect on the temperature gradient region reaction, because only weak compression/acoustic waves are emitted from the plateau's reaction. With only minor heating of the gradient region, the results are nearly identical to the gradient only case. An uncoupled shock wave and chemical reaction are formed and the reaction begins to terminate.

The partially confined and confined cases, shown in Fig. 5.5(c)-5.5(f), both create detonations. The maximum pressure rise in the color bar shown in Fig. 5.5(d) and 5.5(f) is limited to 6 in order to better visualize regions other than the sharp peak at the von Neumann spike. In reality the peak values approach 11.5. The behavior in these cases closely represents that shown by Jackson et al. [31]. The spatial structure of the hot spots studied by Jackson et al. were less important because the case with the gradient in the center established a constant volume reaction. However, the gradient considered in this work is just short of causing a detonation, making the structure of the hot spot and acoustic timescale of the plateau region of paramount importance.

Figures 5.5(c) and 5.5(d) show the results for the partially confined case with a plateau timescale ratio of $\tau_e/t_a = 1$. The pressure rise from the plateau causes the shock to couple with the chemical reaction, amplifies the reaction, and eventually forms a detonation wave. This coupling is apparent in Fig. 5.5 (d) as the white dashed line lies on the shock wave location until $(t - \tau_i^v)/\tau_e^v \approx 14$. The accelerative nature of the reaction may also be seen in the dashed line in these figures by observing that the slope decreases with time when the shock and reaction are coupled. After $(t - \tau_i^v)/\tau_e^v > 14$, the shock wave and reaction decouple because the temperature drops below a level capable of sustaining a detonation.

Figures 5.5(e) and 5.5(f) show results for the confined case. This case creates a detonation earlier than the partially confined case. The x-t diagrams show that a detonation is formed around $(t - \tau_i^v)/\tau_e^v \approx 11$ for the partially confined case, and approximately $(t - \tau_i^v)/\tau_e^v \approx 7.5$ in the confined case. Apart from this earlier detonation formation, the two cases are very similar.

Figure 5.6 shows the x-t diagram of the Mach number for each case. In the gradient only case, a shock wave created by the initial fluid reaction induces an $O(1)$ Mach number. Adding an unconfined plateau to this results in a slightly higher Mach number, but ultimately the behavior is similar. Figures 5.6(c) and 5.6(d) show Mach contours for the partially confined and confined cases, respectively. Both result in a detonation, inducing a supersonic fluid velocity immediately behind the detonation front.

Figure 5.7 shows the half-reaction location, $x_{1/2} = x(Y = 0.5)$, and reaction propagation velocity normalized by the reference sound speed, a_o for each temperature gradient case. The reaction propagation velocity is defined as the instantaneous rate of change of the half-reaction location, $u_s = dx_{1/2}/dt$. As the reaction propagates into the domain, the wave accelerates until it reaches a maximum velocity after which it decelerates due to low initial temperatures. The gradient only case is the slowest reaction and travels the smallest distance into the domain. Alternatively, the confined and partially confined cases both have the largest velocities (at separate times) and travel progressively further into the domain. The plateau regions are consumed relatively uniformly, which causes the large jump in half-reaction location and propagation velocity (most notable in the confined case).

Figure 5.7(a) shows that the reaction in the gradient only case ($l_p = 0$) never couples with the shock and does not form a detonation. Figure 5.7(b) shows that the reaction propagation

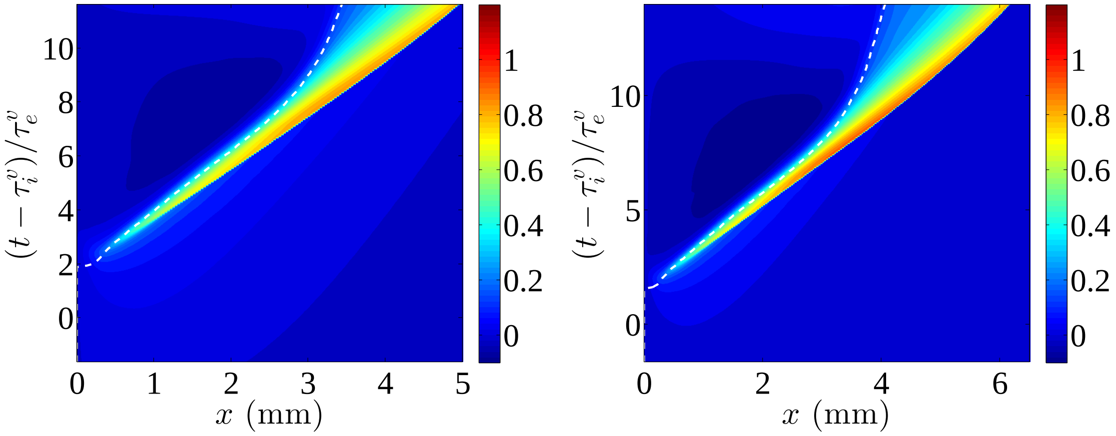

(a) Gradient Only: $l_p = 0$

(b) Unconfined: $\tau_e/t_a = 10$

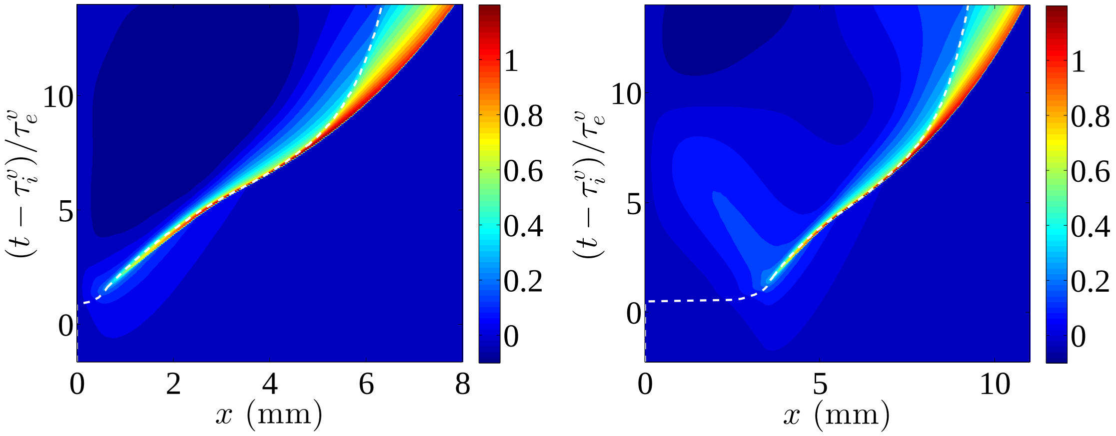

(c) Partially confined: $\tau_e/t_a = 1$

(d) Confined: $\tau_e/t_a = 0.1$

Figure 5.6 x-t diagrams of Mach number for each gradient with plateau model case.

velocity for the unconfined case increases slightly relative to the gradient only case, but overall behaves similarly. The partially confined, and confined cases both form detonations. In these cases the compression and shock waves preheat the reactive mixture inside the temperature gradient region. This shortens the ignition delay time such that the reaction couples with the compression/shock waves to form a detonation. The peak in propagation velocity occurs sooner for the confined case than the partially confined case, which shows the compressive heating from the plateau reaction significantly increases the reaction rate in the gradient region. An additional case with $\tau_e/t_a = 0.01$ was performed. However, the results are identical to the $\tau_e/t_a = 0.01$ case. This suggests that the cases presented fully capture the range of thermomechanical responses possible from this coupled behavior.

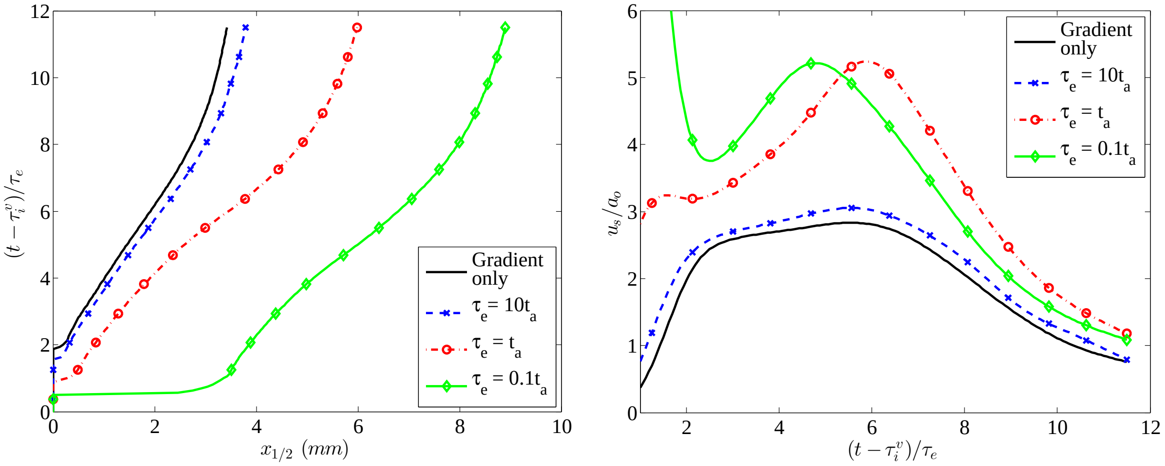

(a) Half-reaction location for each case (b) Propagation velocity for each case

Figure 5.7 Comparison of half-reaction location and propagation velocity for each gradient with plateau model case.

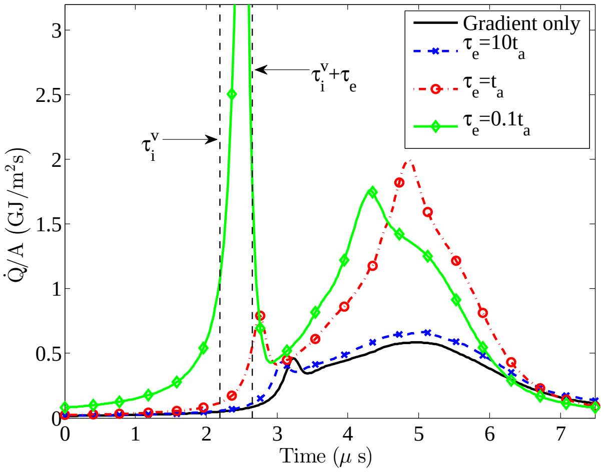

Figure 5.8 Comparison of global heat release per unit area ($\dot{Q}$/A) for each gradient with plateau model case.

The velocity in the gradient only case at $t = 0$ is roughly equal to the spontaneous wave speed described in Zeldovich, [38] $u_s = (d\tau_i/dx)^{-1}$. However, it rapidly increases due to compressive heating, which is not accounted for in the pure kinetics of Zeldovich's study. As expected, since the Zeldovich mechanism [11, 38] does not account for gasdynamic heating, it significantly underpredicts the spontaneous wave speed for all cases.

It is common to compare cases using the globally integrated, instantaneous heat release as a function of time. As done in previous work [32, 33, 34], the chemical heat release rate integrated over the fluid volume, $\forall$, at each time instant t, is defined

$$\dot{Q}(t) = \int_{\forall} \dot{W}(t) q d\forall\,. \tag{5.1}$$

In 1D, this is analogous to the global heat release per unit area integrated over the domain length,

$$\frac{\dot{Q}(t)}{A} = \int_{l_p+l_g} \dot{W}(t) q dx. \tag{5.2}$$

The global heat release per unit area is plotted in Fig. 5.8 for each plateau with gradient case. Two vertical dashed lines represent the ignition delay time, τ_i^v, and the sum of the ignition delay and excitation times, $\tau_i^v + \tau_e^v$, to show the beginning and end of the plateau reaction for an isochoric reactor. These align with a large spike in global heat release in the confined case. The vertical axis has been limited to show detail in all cases, but the spike in $\dot{\mathrm{Q}}$ reaches a value of 5.9 GJ/m^{2}s for the confined case. A similar spike can be seen in each case, even the gradient only case. This is due to the non-linear nature of the ignition delay time. As the temperature increases linearly near the top of the gradient, the ignition delay time asymptotes to a constant value. Thus, a small volume of fluid towards the top of the gradient reacts at nearly the same time, acting as a type of thermal plateau.

The unconfined case does not cause the magnitude of this spike to increase, but it does shift the time of this spike to around $t = 3.1\ \mu s$. The partially confined case causes a larger spike in heat release even earlier at $t = 2.8\ \mu s$, slightly earlier than the gradient only case. After these initial plateau reactions, the global heat release reduces to a local minimum. It then increases to some local maximum as the reaction progresses down the gradient. As the initial temperature continues to get lower, the reaction slows, resulting in a decreasing region of heat release.

5.1.3 Variable gradient and plateau lengths

The results within this section expand upon Sec. 5.1.2 by varying the temperature gradient length l_g. Equation 2.14 shows the relationship between plateau length and acoustic timescale ratio can be written $l_p/L = t_a/\tau_e$. As the plateau length increases, the acoustic timescale ratio decreases, resulting in a more inertially confined plateau reaction. The gradient and plateau

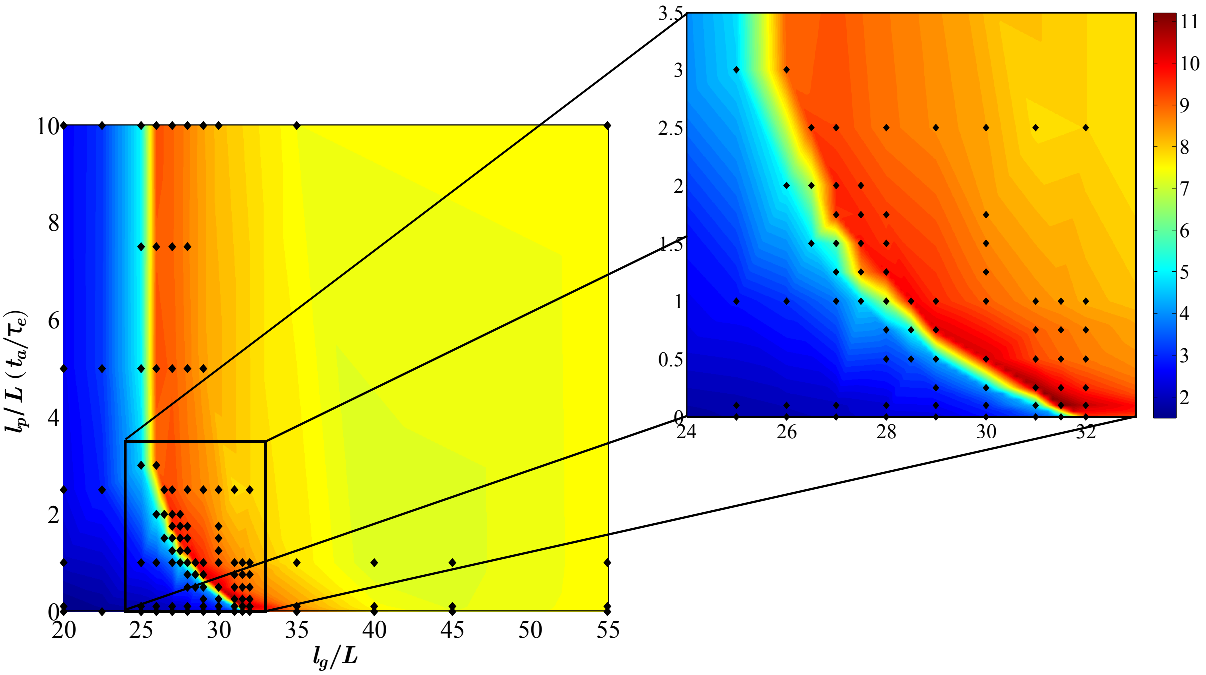

Figure 5.9 x-t diagrams of temperature and pressure for the gradient with plateau cases.

sizes considered are within the domains $20L \leq l_g \leq 55L$ and $0 \leq l_p \leq 100L$, respectively. The results from this two parameter study are presented as contour plots of the maximum pressure rise in Fig. 5.1.3. The black diamonds correspond to the cases that are run computationally. A linear interpolation is used to fill in areas that are not run explicitly. The gradient length is on the horizontal axis and plateau length l_p is on the vertical axis. Both lengths are normalized by the reaction length scale, L.

Figure 5.1.3 shows most of the parameter space, as well as close-up view. Plateau lengths greater than $10L$ are not shown since the results behave similarly to $l_p = 10L$. The results from the previous section show that adding a temperature plateau can enhance the reaction of a surrounding temperature gradient, depending on whether the plateau reacts at constant volume, constant pressure, or somewhere inbetween. Figure 5.1.3 demonstrates this effect well, showing that the detonability of a hot spot within this parameter space forms a continuous curve.

In the gradient only cases, $l_p \to 0$, a detonation is not formed below $l_g = 32L$. Cases with $26L < l_g < 32L$ can form a detonation when a plateau is added, depending on its size. A plateau of length $3L$ will create a detonation for any gradient within this range ($26L < l_g < 32L$).

Plateaus with lengths greater than $3L$ have the same effect upon the surrounding gradient as a plateau of length $3L$. This is because they are reacting in a near constant volume fashion, resulting in the same thermomechanical behavior, and hence, have the same effect upon the surrounding gradient. To this point, Fig. 5.1.3 shows that a detonation with the same maximum pressure forms for every gradient length within the range $26L < l_g < 32L$ when a plateau of length $3L$-$10L$ is added.

The detonability is more dynamic with plateau lengths less than $3L$, as seen in Fig. 5.1.3. Plateaus of length $l_p = L$ in combination with a gradient will create a detonation only when $l_g > 28L$. A plateau with $l_p = 0.1L$ will cause a detonation only when combined with a gradient of length $l_g > 31.5L$. These observations behave as expected and frame the outline of this parameter space. Overall, as the gradient length is decreased (gradient slope becomes steeper) larger plateaus are required to form a detonation wave.

5.2 Two Dimensional Results

The symmetric cases are presented first to study the multidimensional effects independent of asymmetry effects. Results for the square cases are expected to behave in a relatively planar fashion on the x- and y-axes, prior to the acoustic time. Additional expansion in the circular cases is expected to lessen this effect. In Sec. 5.2.2 the effect of asymmetry is explored by altering the aspect ratio between t_a^y and t_a^x for both rectangular and elliptical models. As the aspect ratio becomes larger, 1-D behavior along the shorter axis is expected to occur for a longer time period.

In each section a series of temperature contours from select cases are presented to show the hot spot reaction and illustrate its evolution. Due to the qualitative nature of the information conveyed with these contours, only one case from each model will be presented. After this, it is most constructive to view results from a 1-D slice along the shorter axis (x-axis), where a direct comparison with 1-D results can be made. Each section will investigate the 2-D rectangular model first to directly compare with 1-D results. The results from the more realistic elliptical model are presented second.

5.2.1 Effects of Multiple Dimensions

To study the effects of multiple dimensions, four symmetric ($t_a^x = t_a^y = t_a$) cases are considered with each model (square and circular). First, a case is run with no plateau region ($l_x = l_y = 0$) to establish the baseline behavior of the temperature gradient in 2-D. This will be referred to as the "gradient only" case. Three other cases are examined with acoustic timescale ratios of $\tau_e/t_a = 10, 1,$ and 0.1. The $\tau_e = 10t_a$ case will be termed the "unconfined" case, $\tau_e = t_a$ the "partially confined" case, and $\tau_e = 0.1t_a$ the "confined“ case.

5.2.1.1 Square Model

Figure 5.10(a) contains a sequence of temperature contours displaying the hot spot evolution of the confined case ($\tau_e/t_a = 0.1$) for the square model. A blue line is superimposed on the location of half-reaction to show the reaction progress. The simulation time has been

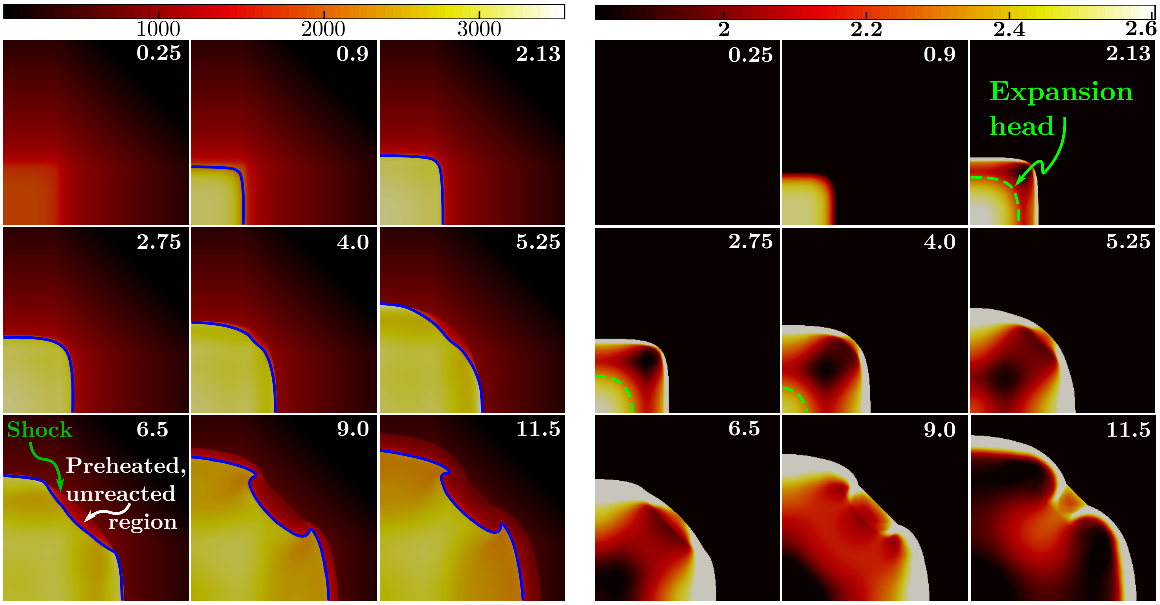

(a) Temperature (K) (b) Pressure (p/p$_o$)

Figure 5.10 Select time steps of temperature contours for the (a) Temperature (K) and (b) Pressure (p/p$_o$) for the square case with $\tau_e/t_a = 0.1$. Time in upper-right corner of each frame is normalized time, $(t - \tau_i)/\tau_e$.

shifted by the ignition delay period τ_i, normalized by the excitation time τ_e, and is labeled at the top right of each frame. Unreacted fuel mixture appears red, while combustion products are yellow. A shock wave can be seen as the temperature discontinuity it creates.

For $0.9 < (t - \tau_i)/\tau_e < 2.75$ in Fig. 5.10(a), the half-reaction location (blue line) coincides with the burnt-unburnt gas interface. This suggests that the reaction is coupled with the shock that is formed from the consumption of the reactants in the plateau region. At $(t - \tau_i)/\tau_e = 4.0$ the reaction front is no longer coupled with the shock everywhere in the domain and by $(t - \tau_i)/\tau_e = 6.5$ there is clear separation of the fluid that is preheated from the shock and the burnt combustion products as indicated in the figure. For $0 < (t - \tau_i)/\tau_e \leq 6.5$ the shock and reaction are coincident along the x- and y-axes, which indicates the wave is propagating as a detonation in those regions. At $(t - \tau_i)/\tau_e = 9.0$, the shock and reaction fronts decouple along the x- and y-axes too. Unlike the 1-D analysis that shows detonation formation for both the confined ($\tau_e/t_a = 0.1$) and partially confined ($\tau_e/t_a = 1$) cases, only the confined case results in detonation formation in two dimensions.

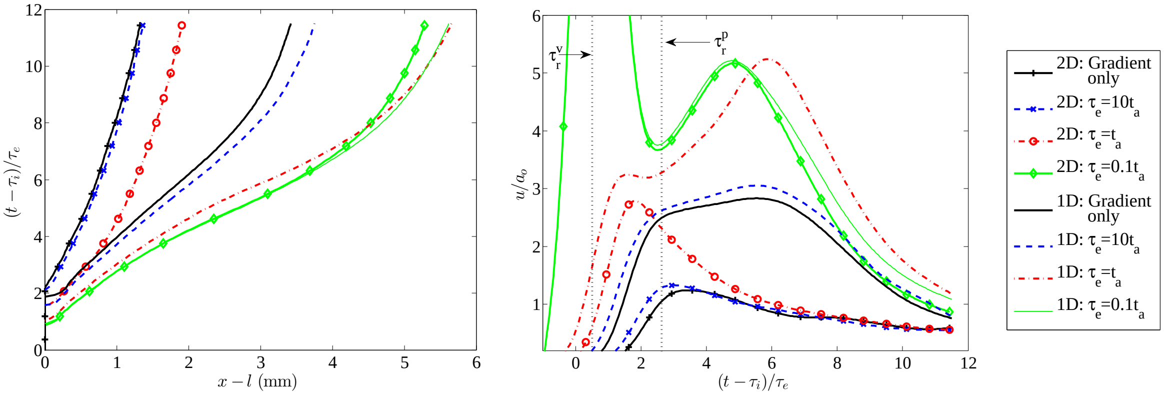

(a) Half-reaction location

(b) Propagation velocity

Figure 5.11 Square model: comparison of half-reaction location and propagation velocity of reaction wave along the x-axis of all 2-D cases. Corresponding 1-D cases are included with the same line style and color sans markers. Two vertical dotted lines are included to represent the reaction times for an isochoric, τ_r^v, and isobaric, τ_r^p, homogeneous reactor.

Figure 5.10(b) shows the corresponding confined case pressure contours. Upon reaction of the plateau region at $(t - \tau_i)/\tau_e = 1$, compression and expansion waves, observed first in frame $(t - \tau_i)/\tau_e = 2.13$, travel outwards and inwards from the edge of the plateau region. As expected, these waves are mostly planar initially. At $(t - \tau_i)/\tau_e = 2.13$, Fig. 5.10(b) shows this planar behavior. The head of the inward traveling expansion wave, defined as the location the pressure has decreased to 90% of the isochoric plateau reaction temperature, is marked by a green dashed curve. If the expansion wave is assumed to travel at the speed of sound through combustion products that are at the isochoric post-combustion temperature, the expansion wave will reach the center of the hot spot at $(t - \tau_i)/\tau_e = 4.8$. Figure 5.10(b) shows that the expansion wave does reach the center in that time, as indicated by the green line disappearing between frames 4.0 and 5.25.

The behavior of the partially confined, unconfined, and gradient only cases is best illustrated by plotting the half-reaction location on the axes and the speed of the spontaneous wave relative to the 1-D cases. Figure 5.11 shows the half-reaction location shifted by the plateau size, $x_{1/2} - l = x(Y = 0.5) - l$, and reaction propagation velocity, $u_s = dx_{1/2}/dt$, normalized by the reference sound speed, a_o along the x-axis for each square case. 1-D cases with corresponding plateau acoustic timescales are included with the same line style, without line markers. The time axis is shifted by the ignition delay time and normalized by excitation time so that zero corresponds to the end of the ignition delay time and one corresponds to the end of the reaction.

Two vertical dotted lines are included in the velocity plot representing the reaction times, defined $\tau_r = \tau_i + \tau_e/2$, for isochoric, τ_r^v, and isobaric, τ_r^p, homogeneous reactors. These times align well with the initial peak in velocity that occurs due to the reaction of the confined and unconfined plateaus, respectively. As expected, this suggests the confined plateau reacts in a constant volume process and the unconfined plateau in a nearly constant pressure process. The addition of a larger plateau causes a larger volume of fluid to react more quickly, resulting in a more confined reaction, and a larger initial transient propagation velocity. After the plateau reacts the reaction wave either accelerates until it reaches a maximum velocity after which it decelerates due to low initial temperatures, or it decelerates immediately.

As illustrated in Fig. 5.11(a), the gradient only case has the slowest traveling reaction wave and penetrates the smallest distance into the domain. Alternatively, the confined case has the largest velocity and travels farthest into the domain. Overall, the additional dimension allows the fluid to expand in a direction orthogonal to the direction of reaction wave propagation. This extra expansion reduces the inertial confinement of the system and results in a reaction process that takes longer. As can be expected, this suggests that in multiple dimensions a shallower gradient is required to form a detonation.

In addition, the 1-D behavior observed from adding a plateau region to a gradient is also observed in these 2-D cases. Namely, more confined plateaus will react quicker, emit stronger compression waves, and cause the reaction to propagate further into the domain at a larger velocity. This effect is seen in Fig. 5.11 as increasingly confined plateaus (τ_e/t_a decreasing) are added to the gradient. Since the 1-D gradient only case is much closer to forming a detonation alone, the addition of a partially confined plateau causes it to detonate, whereas a confined plateau is required to form a detonation with this slope in 2-D.

When the excitation time is much smaller than the acoustic time, as in the confined case ($\tau_e = 0.1 t_a$), the inward traveling expansion will reach the center of the plateau well after the reaction is complete. This occurs at $(t - \tau_i)/\tau_e = 4.8$, which is consistent with what is observed in Fig. 5.10(b) where the expansion head disappears between frames 4.0 and 5.25. Figure

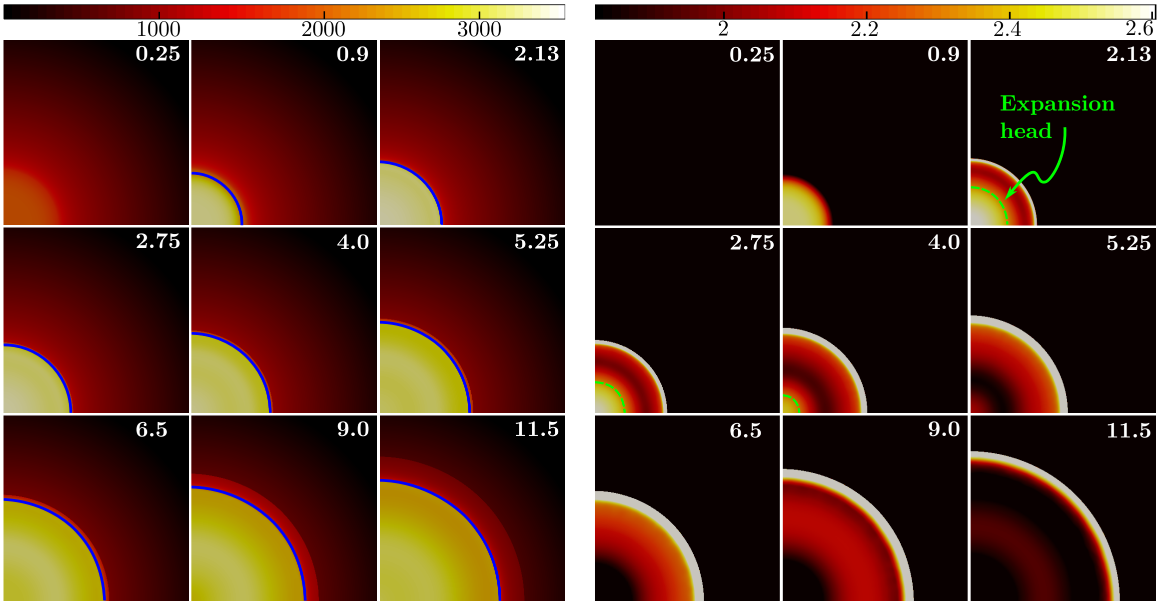

(a) Temperature (K)   (b) Pressure (p/p$_o$)

Figure 5.12 Select time steps of temperature contours for the (a) Temperature (K) and (b) Pressure (p/p$_o$) for the circular case with $\tau_e/t_a = 0.1$. Time in upper-right corner of each frame is normalized time, $(t - \tau_i)/\tau_e$.

5.11(b) shows that after this time, two-dimensional expansion effects come into play, causing the reaction to decelerate and separate from the 1-D result. This means the symmetry axes for 2-D hot spots behave similarly to the 1-D hot spots until the expansion wave has reached the center. Once the expansion wave has reached the center, multidimensional expansion causes the reaction to occur more slowly than the 1-D model.

5.2.1.2 Circular Model

Here, a more realistic circular plateau is considered, which uses the same four plateau acoustic timescale ratios as the square case. Fig. 5.12(a) contains temperature contours for the circular confined case. The blue line, which indicates the reaction front, is collocated with the temperature discontinuity until $(t - \tau_i)/\tau_e = 4.5$. Since the temperature discontinuity is created by the shock wave, this indicates that the reaction and shock wave are coupled and a detonation wave exists during this time. Figure 5.12(b) provides the corresponding pressure contours. As in the square case, a shock wave propagates outwards and an expansion (marked in frame 2.13) propagates inwards. Here, these two waves have curvature throughout the domain,

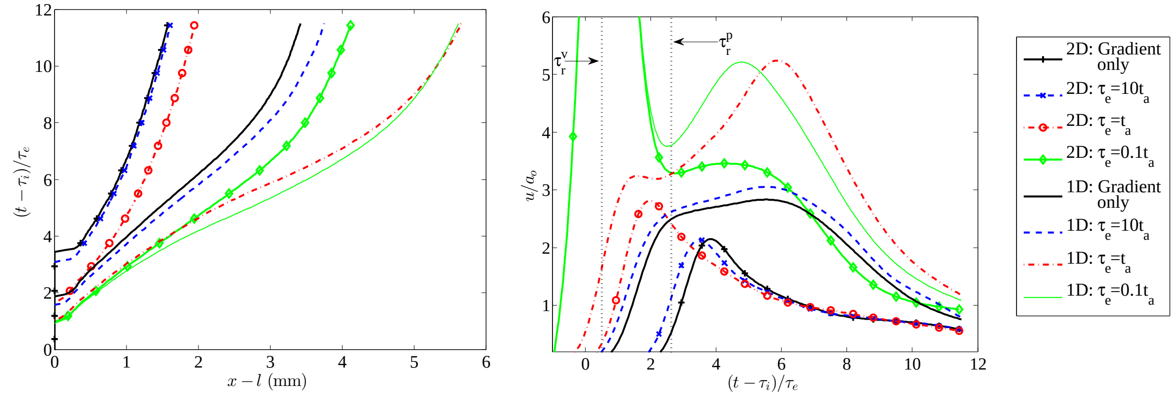

(a) Half-reaction location (b) Propagation velocity

Figure 5.13 Circular model: comparison of half-reaction location, propagation velocity of reaction wave, and global heat release along the x-axis of all 2-D cases. Corresponding 1-D cases are included with the same line style and color sans markers. Two vertical dotted lines are included to represent the reaction times for an isochoric, τ_r^v, and isobaric, τ_r^p, homogeneous reactor.

which is different than square cases where there was a period of time when the expansion waves were planar.

Figure 5.13 shows the half-reaction location and reaction propagation velocity for each circular case. The overall behavior of the circular cases is similar to the square cases. Figure 5.13(b) shows there is a large initial acceleration indicated by the first velocity maximum, after which all 2-D cases decelerate, except for the confined case. This initial maximum is associated with the reaction of the plateau region. The amount of fluid to be consumed in the excitation time, τ_e, for the confined case is much larger than that of the unconfined and partially confined cases. This causes the first maximum in the confined case to be significantly larger than the others.

Figure 5.13(b) shows that once the confined plateau reaction is complete there is a local minimum in propagation velocity (near the vertical line τ_p^r). Following this minimum there is a slight increase in propagation speed, which indicates the propagation of a detonation. The propagation speed reaches a maximum at a time $(t-\tau_i)/\tau_e = 4.25$. For $(t-\tau_i)/\tau_e = 5$, the propagation speed begins to decrease, which indicates that the detonation propagates for only a short period of time before the reaction ceases to be coupled with the shock. The 1-D behavior along the x-axis only lasts until $(t-\tau_i)/\tau_e \approx 2.75$ compared to $(t-\tau_i)/\tau_e \approx 5.25$ seen in the

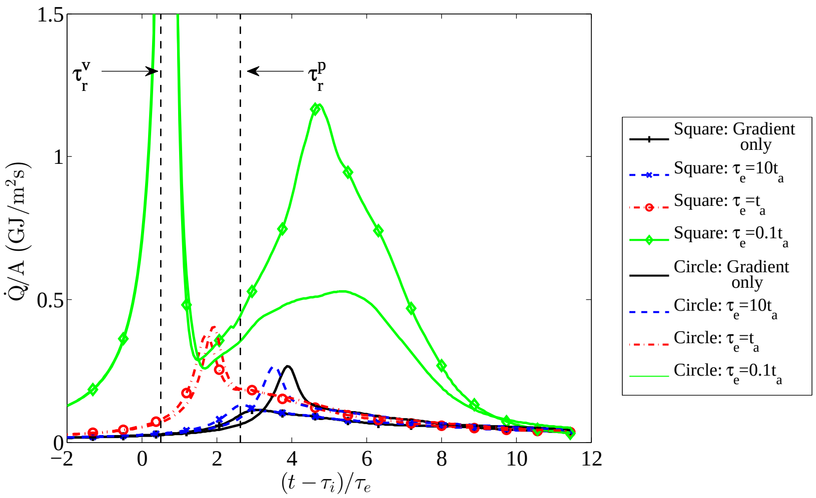

Figure 5.14 Comparison of global heat release along the x-axis of square and circular 2-D cases. Two vertical dotted lines are included to represent the reaction times for an isochoric, τ_r^v, and isobaric, τ_r^p, homogeneous reactor.

square confined case, which shows the additional expansion in the circular case that is not present initially in the square case causes the reaction to proceed more slowly.

It is illustrative to compare the globally integrated instantaneous heat release per unit area, defined as $\dot{Q}(t)/A = \int_{l_p+l_g} \dot{W}(t)q dx$, as a function of time to contrast the different cases. Figure 5.14 shows the global heat release along the x-axis for the circular and square cases. The initial maximum in all cases is due to the plateau reaction, after which the heat release decreases. Both the square and circular confined cases develop into detonations which causes the heat release to increase again after the local minimum that occurs at approximately $(t-\tau_i)/\tau_e = 1.5$. However, additional expansion in the circular confined case causes heat to be released at a slower rate compared to the square confined case, beginning around $(t - \tau_i)/\tau_e = 1.5$.

5.2.2 Asymmetric Effects

The height of the plateau region is increased in both the rectangular and elliptical models to analyze the effect of asymmetry on hot spot reaction. As discussed earlier, the primary focus will be on the partially confined case with the pocket width l_x constructed such that $t_a^x = \tau_e$. The plateau height l_y is increased to raise the aspect ratio between t_a^y and t_a^x. Three cases with $t_a^y/t_a^x = l_y/l_x = 2, 5,$ and 10 are considered with the rectangular and elliptical hot

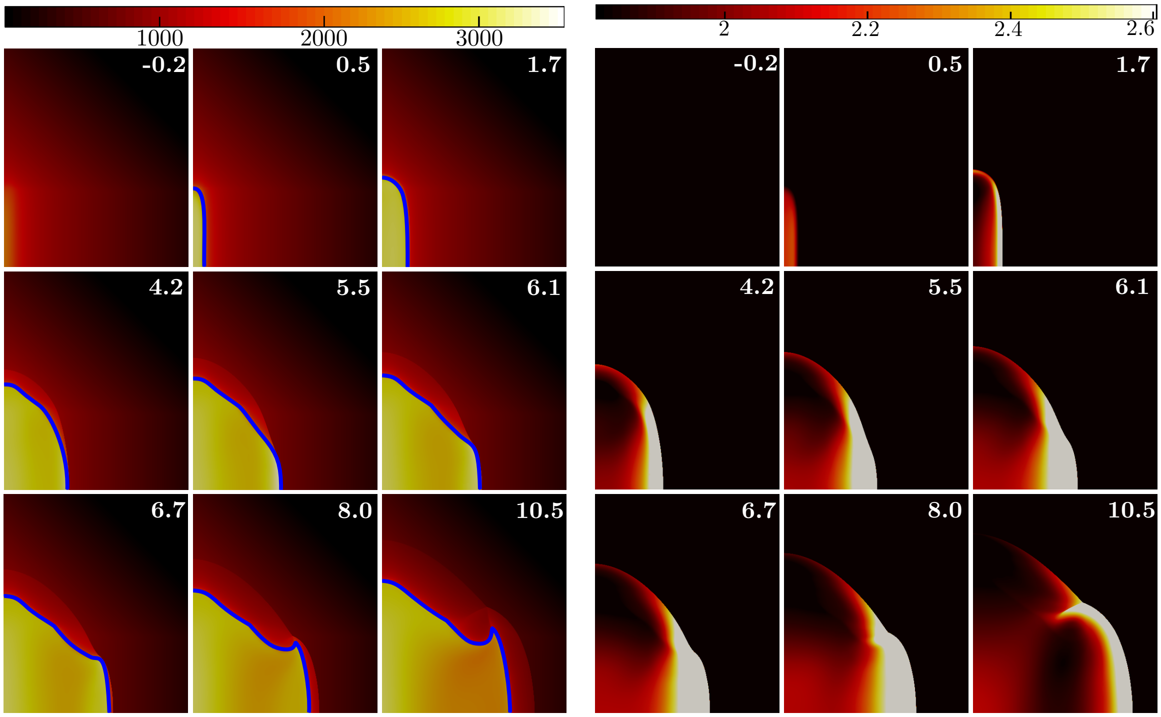

(a) Temperature (K) (b) Pressure (p/p$_o$)

Figure 5.15 Select time steps of (a) Temperature (K) and (b) Pressure (p/p$_o$) contours for the rectangular cases with $t_a^y/t_a^x = 10$. Time in upper-right corner of each frame is normalized time, $(t - \tau_i)/t_a^x$.

spot models to demonstrate the effects of asymmetry. As this ratio is increased, 1-D behavior should be recovered along the short axis until multidimensional expansion slows the reaction. As in the last section, the rectangular model will be investigated first as a direct extension of 1-D, followed by the more realistic elliptical model.

5.2.2.1 Rectangular Model

Figure 5.15 contains a sequence of temperature and pressure contours which show the reaction of the hot spot with aspect ratio $t_a^y = 10t_a^x$ for the rectangular model. The time, labeled at the top right of each frame, has been shifted by the ignition delay time, τ_i, so zero corresponds to the end of the ignition delay period. The time has also been normalized by t_a^x, since all cases have the same acoustic time along the x-axis.

Upon reaction of the plateau region, relatively planar compression and expansion waves are generated in the positive and negative x-directions, respectively. Frame 1.7 in Fig. 5.15(b)

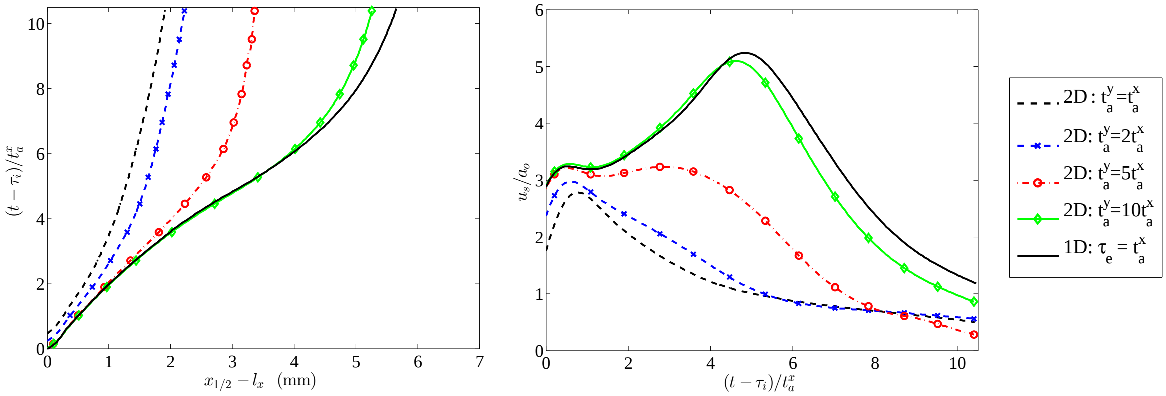

(a) Half-reaction location (b) Propagation velocity

Figure 5.16 Rectangular model: comparison of half-reaction location and propagation velocity of reaction wave along 1-D slice on x-axis for $t_a^y/t_a^x = 2, 5$ and 10 with 1-D results.

shows the compression wave and the expansion wave that is reflected off the left symmetry axis. The large aspect ratio causes a separation of timescales for fluid expansion along the large axis (l_y) and small axis (l_x), resulting in dominant behavior along the short axis. As the reaction progresses, a detonation forms in the x-direction, evident from the shock-coupled reaction seen in frames $4.2 \leq (t-\tau_i)/t_a^x \leq 6.1$ of Fig. 5.15(a). As the reaction decouples from the shock front around $(t-\tau_i)/t_a^x \approx 6.7$, hot reaction products are allowed to expand in the y-direction.

To gain a better understanding of these results, a 1-D slice along the x-axis of each case is now compared with the 1-D results. Figure 5.16 shows the half-reaction location and reaction propagation velocity for the three 2-D rectangular model cases with $t_a^y/t_a^x = 1, 2, 5$ and 10, in addition to the 1-D partially confined case.

The case with $t_a^y = 2t_a^x$ looks similar to the square partially confined case with $t_a^x = t_a^y = t_a$ seen in Fig. 5.16. Fig. 5.16(a) shows that the reaction begins slightly later than the other cases with larger aspect ratios. The half reaction location quickly deviates from 1-D and other higher aspect ratio cases, but it travels further into the domain than the 2-D symmetric case. The case with $t_a^y = 5t_a^x$ behaves like the 1-D case longer than the $t_a^y = 2t_a^x$ case, resulting in the reaction propagating further into the domain (Fig. 5.16(a)) at a larger wave speed, seen in Fig. 5.16(b). Figure 5.16(a) shows that the half-reaction location begins to deviate significantly from the 1-D location when $(t-\tau_i)/t_a^x \approx 3$.

Figure 5.16(a) shows the $t_a^y = 10t_a^x$ case matches the 1-D results the longest, with notable deviations beginning around $(t-\tau_i)/t_a^x = 7$. This causes the reaction wave to propagate the farthest into the domain and have a much larger velocity than the $2t_a^x$ or $5t_a^x$ cases. The $10t_a^x$ case behaves like the 1-D case long enough to form a detonation in the x-direction, just as in the 1-D case. As the aspect ratio is increased, the behavior of the reaction in the direction normal to the larger hot spot axis resembles 1-D behavior, which is expected since the limit of infinite aspect ratio $l_y/l_x \to \infty$ corresponds exactly to the 1-D case. Some deviation prior to t_a^y is seen in Fig. 5.16. This is due to other multidimensional effects, such as rounding of the expansion waves and expansion wave interaction with reflected expansion waves.

5.2.2.2 Elliptical Model

The results of the previous section can be expanded upon by considering a more realistic elliptical asymmetric hot spot. The sequence of temperature and pressure contours in Fig. 5.17(a) and 5.17(b) display the evolution of an elliptical hot spot with $t_a^y = 10t_a^x$. This case results is a shock coupled reaction for times $1.7 \leq (t-\tau_i)/t_a^x \leq 6.7$. This coupling does not last as long as the rectangular case (Fig. 5.15). As the height of the plateau (l_y) increases, the hot spot is elongated. This causes a larger portion of the reaction in the elliptical cases to be orthogonal to the x-axis, which results in behavior similar to the rectangular cases when t_a^y/t_a^x becomes large.

Figure 5.18 shows the half-reaction location and reaction propagation velocity for the elliptical cases with aspect ratio $t_a^y/t_a^x = 1, 2, 5$ and 10 as well as the 1-D partially confined case. Similar to the asymmetric rectangular cases, increasing the aspect ratio causes 1-D behavior along the x-axis for a longer period of time. This results in the reaction wave traveling further into the domain (Fig. 5.18(a)) at a larger velocity (Fig. 5.18(b)). As in the circular cases, there is an extra degree of expansion due to the initial curvature of the plateau region. The difference between the elliptical and rectangular plateau regions is less pronounced than the symmetric cases. The asymmetry causes the elliptical plateau to have a larger planar region than the circular plateau. This causes the curvature effect seen in the circular case to have a smaller effect on the elliptical case, allowing its behavior to be more similar to the asymmetric rectangular cases as the hot spot becomes more elongated.

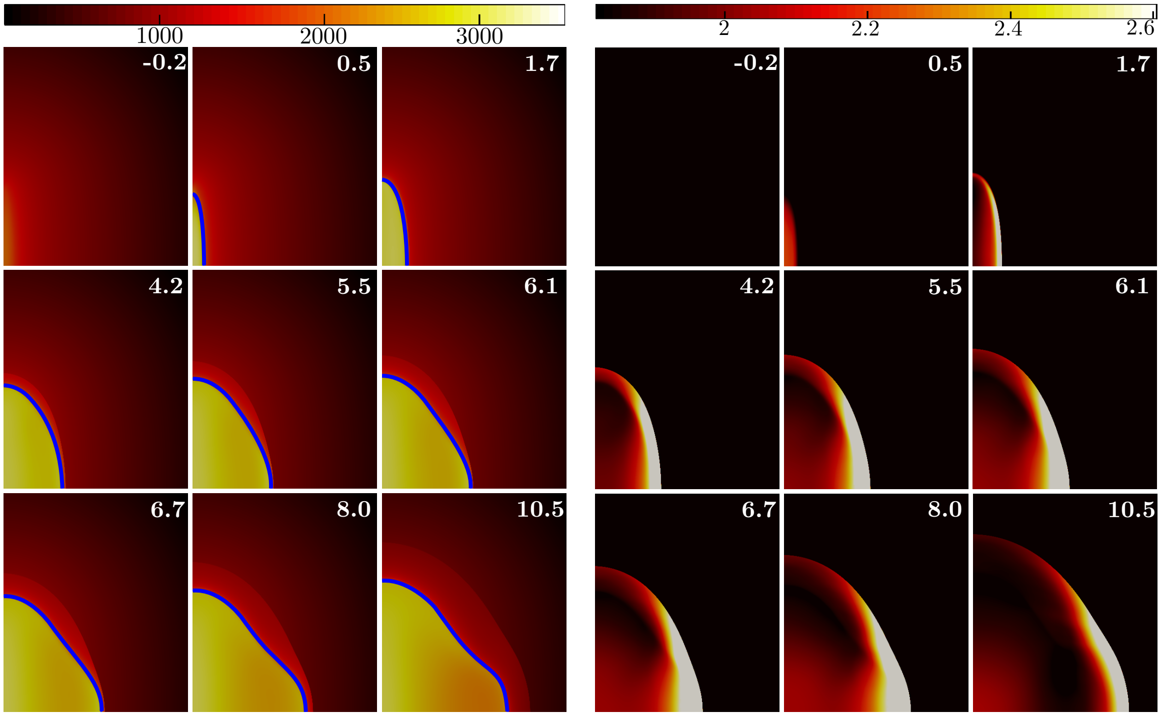

(a) Temperature (K)

(b) Pressure (p/p$_o$)

Figure 5.17 Select time steps of (a) Temperature (K) and (b) Pressure (p/p$_o$) contours for the elliptical cases with $t_a^y/t_a^x = 10$. Time in upper-right corner of each frame is normalized time, $(t - \tau_i)/t_a^x$.

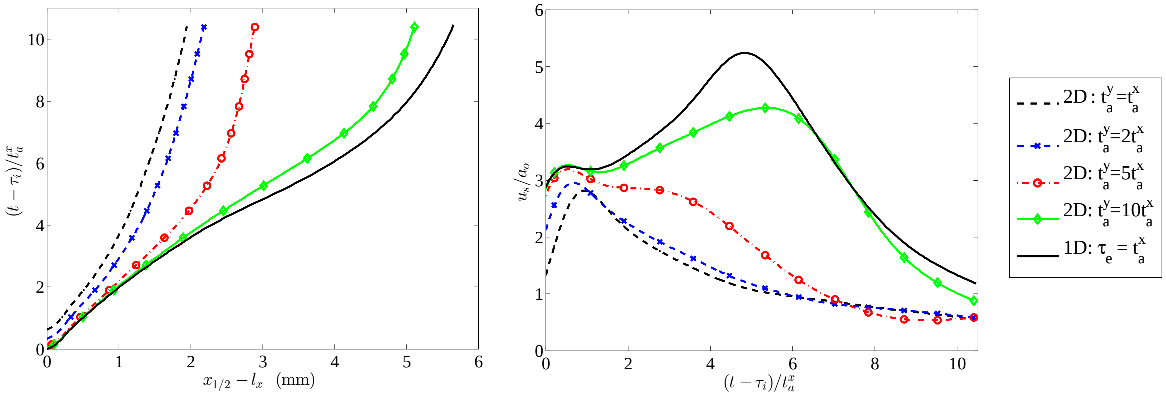

(a) Half-reaction location

(b) Propagation velocity

Figure 5.18 Elliptical model: comparison of half-reaction location and propagation velocity of reaction wave along 1-D slice on x-axis for$t_a^y/t_a^x = 2, 5$ and 10 with 1-D results.

CHAPTER 6. CONCLUSIONS

The half-reaction time of a hot spot is shown to be a function of the length-scale of the hot spot. This half-reaction time is demarcated by the isochoric and isobaric half-reaction times. While the difference between these times is only 30%, there are significantly different fluid dynamic responses depending on hot spot sizes varying over two orders of magnitude.

Hot spots are modeled using temperature plateaus and plateaus combined with a temperature gradient. For plateau only cases, the excitation to acoustic timescale ratio is used to characterize the thermomechanical response of the surrounding fluid. A ratio larger than unity will cause the hot spot to react in a nearly constant pressure process. When the timescales are equal, there will be simultaneous reaction and fluid expansion with the formation of compression waves. If the acoustic time is 10 times the excitation time, the hot spot will be inertially confined, react at a nearly constant volume, and form shock waves. The plateau only hot spot model is insufficient by itself to model the full hot spot behavior. However, it demonstrates the importance of the acoustic time and length scale of the hot spot and how they can be used to characterize the hot spot behavior beforehand.

Simulations are performed to show that temperature plateaus in combination with a linear temperature gradient enhance the detonability of the temperature gradient. Based upon its initial size, a plateau region coupled to a temperature gradient yields different responses when the temperature gradient length is nonzero. Plateaus with $\tau_e \gg t_a$ will react isobarically and have minimal impact on the reaction wave inside the linear temperature gradient. In cases with timescale ratios of order unity compression waves modify the temperature gradient, yielding a different thermo-mechanical response and possibly facilitate detonation formation. A detonation is more likely to form in the confined case ($\tau_e \ll t_a$).

Detonability limits are established for different plateau and temperature gradient lengths.

The two parameter space is continuous and behaves as expected. As the temperature gradient becomes steeper, a larger plateau region is required to form a detonation. These results demonstrate that the spatial structure of an autoignition hot spot can have a significant influence on the reaction wave speed inside the temperature gradient. Furthermore, the acoustic and excitation time scales can be used a priori to characterize the behavior of these model hot spots.

This 1-D hot spot model was extended to two dimensions. Symmetric and asymmetric plateau regions are modeled using both rectangular and elliptical geometries. For symmetric cases, the excitation to acoustic timescale ratio is used to characterize the thermomechanical response of the surrounding fluid. Hot spots with more confined plateaus react quicker, emit stronger compression waves, and cause the reaction to propagate further in the domain at a faster velocity.

In general, the inertial confinement in multiple dimensions is less than that observed in one dimension. It is shown that the effects of additional expansion is most severe in cases with larger plateau acoustic timescale ratios, $\tau_e \gtrsim t_a$, or smaller plateau sizes. However, for cases with significantly small acoustic timescale ratios, $\tau_e \ll t_a$, or large plateau regions, the behavior is very similar to the 1-D model results up to the acoustic time. After the acoustic time, the effects of multidimensional expansion cause the behavior to deviate from the 1-D model.

The effects of asymmetry were studied as well. As the aspect ratio is increased, the behavior along the shorter axis retains 1-D behavior for longer durations. This is due to the the separation of timescales between the two axes. As the aspect ratio is increased, fluid expansion along the long axis takes more time than that of the short axis, which results in dominant, 1-D behavior along the short axis for times before the acoustic time of the long axis. Therefore, when the aspect ratio t_a^y/t_a^x is large, 1-D results become increasingly accurate.

APPENDIX A. NONDIMENSIONALIZATION

The mathematical models used in this work are nondimensionalized using the definitions in Table 2.1. The explicit derivation of the nondimentionalization for the reactive Euler equations, *i.e.*, the mass, momentum, energy, and species conservation equations, in addition to the state equation, sound speed, and internal energy is outlined below.

Mass Conservation

The dimensional form of mass conservation can be written

$$\frac{\partial \rho'}{\partial t'} + \frac{\partial(\rho' u')}{\partial x'} = 0, \tag{A.1}$$

where

$$\frac{\partial}{\partial t'} = \frac{\partial}{\partial t}\frac{\partial t}{\partial t'} = \frac{a_o'}{l'}\frac{\partial}{\partial t} \tag{A.2}$$

and

$$\frac{\partial}{\partial x'} = \frac{\partial}{\partial x}\frac{\partial x}{\partial x'} = \frac{1}{l'}\frac{\partial}{\partial x}. \tag{A.3}$$

Substituting these into Eq. A.1 along with values from Table 2.1 gives

$$\frac{a_o'}{l'}\frac{\partial \rho_o' \rho}{\partial t} + \frac{1}{l'}\frac{\partial(\rho_o' a_o' \rho u)}{\partial x} = 0, \tag{A.4}$$

which can be simplified to

$$\frac{\rho_o' a_o'}{l'}\frac{\partial \rho}{\partial t} + \frac{\rho_o' a_o'}{l'}\frac{\partial(\rho u)}{\partial x} = 0, \tag{A.5}$$

and finally the nondimensional form is written as

$$\frac{\partial \rho}{\partial t} + \frac{\partial(\rho u)}{\partial x} = 0 \tag{A.6}$$

Momentum Conservation

Similarly to mass conservation, the dimensional form of the momentum conservation equation can be written

$$\frac{\partial \rho' u'}{\partial t'} + \frac{\partial(\rho' u'^2 + p')}{\partial x'} = 0. \tag{A.7}$$

Using Eq. A.2 and A.3 along with values from Table 2.1, this can be rewritten as

$$\frac{a'_o}{l'}\frac{\partial(\rho'_o a'_o \rho u)}{\partial t} + \frac{1}{l'}\frac{\partial(\rho'_o a'^2_o \rho u^2 + \rho'_o a'^2_o p)}{\partial x} = 0 \tag{A.8}$$

and simplified to

$$\frac{\rho'_o a'^2_o}{l'}\frac{\partial \rho u}{\partial t} + \frac{\rho'_o a'^2_o}{l'}\frac{\partial(\rho u^2 + p)}{\partial x} = 0 \tag{A.9}$$

which finally reduces to the nondimensional form of the momentum equation,

$$\frac{\partial \rho u}{\partial t} + \frac{\partial(\rho u^2 + p)}{\partial x} = 0. \tag{A.10}$$

Energy Conservation

The energy equation in dimensional form is

$$\frac{\partial \rho' e'_t}{\partial t'} + \frac{\partial(\rho' e'_t + p')u'}{\partial x'} = \dot{Q}', \tag{A.11}$$

where $\dot{Q}'$ is an energy deposition term that is not used in this work. The $\dot{W}q$ term usually seen on the RHS is acounted in the definition of total energy (Eq. 2.7). Again, using Eq. A.2 and A.3 along with values from Table 2.1, this can be rewritten as

$$\frac{a'_o}{l'}\frac{\partial \rho'_o a'^2_o \rho e_t}{\partial t} + \frac{1}{l'}\frac{\partial(\rho'_o a'^2_o \rho e_t + \rho'_o a'^2_o p)u a'_o}{\partial x} = \left(\frac{\rho'_o a'^2_o}{t'_a}\right)\dot{Q}, \tag{A.12}$$

which reduces to

$$\left(\frac{\rho'_o a'^3_o}{l'}\right)\frac{\partial \rho e_t}{\partial t} + \left(\frac{\rho'_o a'^3_o}{l'}\right)\frac{\partial(\rho e_t + p)u}{\partial x} = \left(\frac{\rho'_o a'^3_o}{l'}\right)\dot{Q}, \tag{A.13}$$

and

$$\frac{\partial \rho e_t}{\partial t} + \frac{\partial(\rho e_t + p)u}{\partial x} = \dot{Q}. \tag{A.14}$$

Species Conservation

Similarly, the species can be written in dimensional form as

$$\frac{\partial \rho' Y}{\partial t'} + \frac{\partial (\rho' Y u')}{\partial x'} = -\dot{W}'. \tag{A.15}$$

using Eq. A.2 and A.3 andTable 2.1, this can be rewritten as

$$\frac{a'_o}{l'}\frac{\partial \rho'_o \rho Y}{\partial t} + \frac{1}{l'}\frac{\partial (\rho'_o a'_o \rho Y u)}{\partial x} = -\left(B' \rho' Y e^{-E'/R'T'}\right), \tag{A.16}$$

$$\frac{\rho'_o a'_o}{l'}\frac{\partial \rho Y}{\partial t} + \frac{\rho'_o a'_o}{l'}\frac{\partial (\rho Y u)}{\partial x} = -\left(\frac{\rho'_o a'_o}{l'} B \rho Y e^{-E\gamma R' T'_o / T \gamma R' T'_o}\right), \tag{A.17}$$

$$\left(\frac{\rho'_o a'_o}{l'}\right)\left(\frac{\partial \rho Y}{\partial t} + \frac{\partial (\rho Y u)}{\partial x}\right) = -\left(\frac{\rho'_o a'_o}{l'}\right)\left(B \rho Y e^{-E/T}\right), \tag{A.18}$$

and

$$\frac{\partial \rho Y}{\partial t} + \frac{\partial (\rho Y u)}{\partial x} = -\dot{W}. \tag{A.19}$$

Additional nondimensionalized equations

In addition to the reactive Euler equations, it is pertinent to show additional nondimensionalizations. Namely, the state equation, sound speed and internal energy.

Equation of State

The equation of state, in dimensional form, is

$$p' = \rho' R' T'. \tag{A.20}$$

As done previously, Table 2.1 is used to substitute nondimensionalized variables, giving

$$p \rho'_o a'^2_o = \rho \rho'_o R' T \gamma T'_o, \tag{A.21}$$

$$p \rho'_o (\gamma R' T'_o) = \rho \rho'_o R' T \gamma T'_o, \tag{A.22}$$

and finally, in nondimensional form,

$$p = \rho T. \tag{A.23}$$

Sound Speed

The speed of sound, is

$$a = a'/a'_o. \tag{A.24}$$

This simplifies to

$$a = \sqrt{\gamma R'T'}/\sqrt{\gamma R'T'_o}, \tag{A.25}$$

$$a = \sqrt{\gamma R'(T\gamma T'_o)}/\sqrt{\gamma R'T'_o}, \tag{A.26}$$

and finally, in nondimensional form,

$$a = \sqrt{\gamma T}. \tag{A.27}$$

Internal Engergy

Internal energy is given by

$$e' = C'_v T' = \frac{R'}{(\gamma - 1)} T' \tag{A.28}$$

in dimensional form, which simplifies to

$$e a'^2_o = e(\gamma R'T'_o) = \frac{\gamma R'T'_o}{(\gamma - 1)} T, \tag{A.29}$$

and finally,

$$e = \frac{T}{(\gamma - 1)}. \tag{A.30}$$

APPENDIX B. SPATIALLY HOMOGENEOUS REACTOR - H_2-AIR

Consider a volume of reactive mixture at intitial temperature, T_1. The stoichiometric combustion of a Hydrogen-air mixture

$$H_2 + \frac{1}{2}\left(O_2 + 3.76N_2\right) \rightarrow H_2O + 3.76\left(\frac{1}{2}\right)N_2 \tag{B.1}$$

is modeled using a simple one-step global reaction, Reactants (R) → Products (P), ignoring any detailed kinetics. The rate at which the fuel is consumed can be modeled with a one-step Arrhenius reaction rate. The parameters used in this work are obtained from Bane[1] and listed in terms of a reference state in Table 3.1. In nondimensional form, this rate is given by

$$\frac{dY}{dt} = -B\rho Y(t)exp(-E_a/T(Y)), \tag{B.2}$$

where q is the nondimensional heat of reaction, the fuel mass fraction, $Y(t)$ is a function of time, and the temperature, $T(Y)$ is a function of fuel mass fraction. This function can vary depending on what type of reaction is being modeled, *i.e.*, isohoric or isobaric.

The reaction rate ODE, Eq. B.2, can be solved numerically for $Y(t)$ using one of the models for temperature described below. This gives a distribution of fuel mass fraction over time that can be used to find τ_i, τ_r, and τ_e for either an isochoric or isobaric reaction. Figure B.1 shows how initial temperature affects τ_i and τ_e for a spatially homogeneous isochoric reactor. As expected, increasing initial temperature reduces these times. It is worth noting that the temperatrue has a more significan effect upon the ignition delay time than the excitation time.

Isobaric reactor

For a constant pressure reaction, enthalpy will be conserved throughout the reaction, giving

$$h = h_1 + q(1 - Y), \tag{B.3}$$

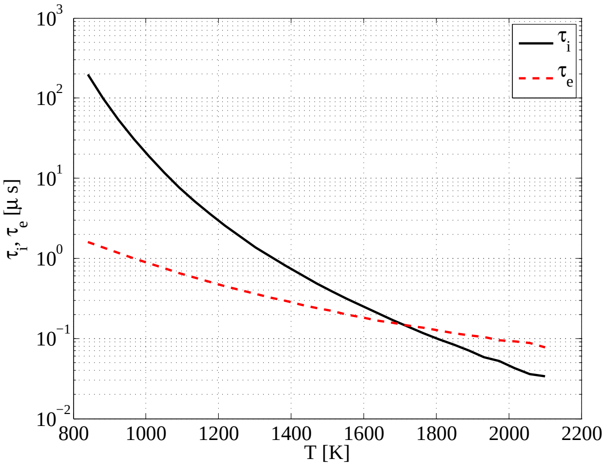

Figure B.1 τ_i and τ_e calculated for a isochoric spatially homogeneous reactor.

where

$$h = e + p/\rho. \tag{B.4}$$

Substituting Eq. B.4 into B.3 and using the non dimensional equation of state, $p/\rho = T = (\gamma - 1)e$, the temperature as a funtion of fuel mass fraction is obtained as,

$$T^p(Y) = T_1 + \frac{(\gamma - 1)}{\gamma} q(1 - Y). \tag{B.5}$$

This corresponds to a maximum temperature

$$T^p_{\text{max}} = T_1 + \frac{(\gamma - 1)}{\gamma} q \tag{B.6}$$

for a isobaric reaction after all fuel is consumed.

Isochoric reactor

Alternatively, temperature for a constant volume reaction can be found using conservation of total energy,

$$e_T = e_{T1} + q(1 - Y). \tag{B.7}$$

where

$$e_T = e + \frac{1}{2}\rho u^2. \tag{B.8}$$

Substituting Eq. B.8 into B.7, $u = 0$ for an isochoric reaction, and using the nondimensional equation of state, the temperature can be expressed as

$$T^v(Y) = T_1 + (\gamma - 1)q(1 - Y). \tag{B.9}$$

This corresponds to a maximum temperature

$$T^v_{\max} = T_1 + (\gamma - 1)q \tag{B.10}$$

for a isochoric reaction.

BIBLIOGRAPHY

[1] Bane, S. P. M., *Spark Ignition: Experimental and Numerical Investigation With Application to Aviation Safety*, Ph.D. thesis, 2010.

[2] Strehlow, R. A., *Combustion Fundamentals*, McGraw Hill, 1989.

[3] Oppenheim, A. K., *Introduction to Gasdynamics of Explosions*, 1970.

[4] Berthelot, M. and Vieille, P., "No Title," *Compt. Rend. Acad. Sci.*, 1881.

[5] Mallard, E. and Chatelier, H. L., "No Title," *Compt. Rend. Acad. Sci.*, Vol. 93, No. 145, 1881.

[6] Chapman, D. L., "On the rate of explosions in gases," *Philosophical Magazine*, Vol. 47, No. 284, 1899, pp. 90–104.

[7] Jouguet, E., "Sur la propagation des réactions chimiques dans les gaz [On the propagation of chemical reactions in gases]," *Journal des Mathématiques Pures et Appliquées*, Vol. 1, No. 6, 1905, pp. 347–425.

[8] Zeldovich, Y. B., "On the theory of the propagation of detonation in gaseous systems," *Journal of Experimental and Theoretical Physics [Ru]; NACA Technical Memorandum 1261 [En] (1950)*, Vol. 10, 1940, pp. 542–568.

[9] von Neumann, J., "Theory of Detonation Waves," *Progress Report No. 238, OSRD No. 549*, , No. May 1942, 1942.

[10] Döring, W., "Über Detonationsvorgang in Gasen [On the detonation process in gases]," *Annalen der Physik [Annals of Physics]*, Vol. 43, 1943, pp. 421–436.

[11] Zeldovich, Y. B., Librovich, V. B., Makhviladze, G. M., and Sivashinskiy, G. I., "On the onset of detonation in a nonuniformly heated gas," *Journal of Applied Mechanics and Technical Physics*, Vol. 11, No. 2, 1970, pp. 264–270.

[12] Lee, J. H. and Moen, I. O., "The mechanism of transition from deflagration to detonation in vapor cloud explosions," *Progress in Energy and Combustion Science*, Vol. 6, No. 4, 1980, pp. 359–389.

[13] Lee, J. H., "Initiation of Gaseous Detonation," *Ann. Rev. Phys. Chem.*, Vol. 28, 1977, pp. 75–104.

[14] Lee, J. H., Knystautas, R., and Yoshikawa, N., "Photochemical initiation of gaseous detonations," *Acta Astronautica*, Vol. 5, 1978, pp. 971–982.

[15] Fickett, W. and Davis, W., *Detonation*, 1979.

[16] Williams, F. A., *Combustion Theory*, The Benjamin/Cummings Punlishing Company, Inc., 1985.

[17] Lee, J. H., *The Detonation Phenomenon*, 2008.

[18] Eckett, C. A., Quirk, J. J., and Shepherd, J. E., "The role of unsteadiness in direct initiation of gaseous detonations," *Journal of Fluid Mechanics*, Vol. 421, Oct. 2000, pp. 147–183.

[19] Radulescu, M. I., Sharpe, G. J., Law, C. K., and Lee, J. H., *The hydrodynamic structure of unstable cellular detonations*, Vol. 580, May 2007.

[20] Shah, A., Brindley, J., McIntosh, A., and Griffiths, J., "Ignition and combustion of low-exothermicity porous materials by a local hotspot," *Proceedings of the Royal Society A: Mathematical, Physical and Engineering Sciences*, Vol. 463, No. 2081, May 2007, pp. 1287–1305.

[21] Oran, E. S. and Khokhlov, A. M., "Deflagrations, hot spots, and the transition to detonation," *Philosophical Transactions of the Royal Society A: Mathematical, Physical and Engineering Sciences*, Vol. 357, No. 1764, Dec. 1999, pp. 3539–3551.

[22] Khokhlov, A. M. and Oran, E. S., "Numerical simulation of detonation initiation in a flame brush: the role of hot spots," *Combustion and Flame*, Vol. 119, No. 4, Dec. 1999, pp. 400–416.

[23] Chen, J. H., Hawkes, E. R., Sankaran, R., Mason, S. D., and Im, H. G., "Direct numerical simulation of ignition front propagation in a constant volume with temperature inhomogeneities I. Fundamental analysis and diagnostics," *Combustion and Flame*, Vol. 145, No. 1-2, April 2006, pp. 128–144.

[24] Sankaran, R. and Im, H. G., "Characteristics of auto-ignition in a stratified iso-octane mixture with exhaust gases under homogeneous charge compression ignition conditions," *Combustion Theory and Modelling*, Vol. 9, No. 3, Aug. 2005, pp. 417–432.

[25] Sankaran, R., Im, H. G., Hawkes, E. R., and Chen, J. H., "The effects of non-uniform temperature distribution on the ignition of a lean homogeneous hydrogen/air mixture," *Proceedings of the Combustion Institute*, Vol. 30, No. 1, Jan. 2005, pp. 875–882.

[26] Merzhanov, A. G., "On Critical Conditions for Thermal Explosion of a Hot Spot," *Combustion and Flame*, Vol. 10, No. 4, 1966, pp. 341–348.

[27] Thomas, P. H., "An Approximate Theory of Hot Spot Criticality," *Combustion and Flame*, Vol. 21, 1973, pp. 99–109.

[28] Zaturska, M. B., "Thermal explosion of interacting hot spots," *Combustion and Flame*, Vol. 25, Aug. 1975, pp. 25–30.

[29] Clarke, J., "Fast flames, waves and detonation," *Progress in Energy and Combustion Science*, Vol. 15, No. 3, Jan. 1989, pp. 241–271.

[30] Nikiforakis, N. and Clarke, J. F., "Quasi-steady structures in the two-dimensional initiation of detonations," Vol. 452, No. 1952, 1996, pp. 2023–2042.

[31] Jackson, T. L., Kapila, A. K., and Stewart, D. S., "Evolution of a Reaction Center in an Explosive Material," *SIAM Journal on Applied Mathematics*, Vol. 49, No. 2, 1989, pp. 432–458.

[32] Sileem, A. A., Kassoy, D. R., and Hayashi, A. K., "Thermally Initiated Detonation through Deflagration to Detonation Transition," *Proceedings of the Royal Society A: Mathematical, Physical and Engineering Sciences*, Vol. 435, No. 1895, Dec. 1991, pp. 459–482.

[33] Kassoy, D. R., Kuehn, J. A., Nabity, M. W., and Clarke, J. F., "Detonation initiation on the microsecond time scale: DDTs," *Combustion Theory and Modelling*, Vol. 12, No. 6, Nov. 2008, pp. 1009–1047.

[34] Regele, J. D., Kassoy, D. R., and Vasilyev, O. V., "Effects of high activation energies on acoustic timescale detonation initiation," *Combustion Theory and Modelling*, Vol. 16, No. 4, Jan. 2012, pp. 650–678.

[35] Regele, J. D., Kassoy, D. R., Vezolainen, A., and Vasilyev, O. V., "Purely Gasdynamic Multidimensional Indirect Detonation Initiation Using Localized Acoustic Timescale Power Deposition," *51st AIAA Aerospace Sciences Meeting*, Vol. 1172, 2013, pp. 1–15.

[36] Regele, J. D., Kassoy, D. R., Vezolainen, a., and Vasilyev, O. V., "Indirect detonation initiation using acoustic timescale thermal power deposition," *Physics of Fluids*, Vol. 25, No. 9, 2013, pp. 091113.

[37] Gu, X., Emerson, D., and Bradley, D., "Modes of reaction front propagation from hot spots," *Combustion and Flame*, Vol. 133, No. 1-2, April 2003, pp. 63–74.

[38] Zeldovich, Y. B., "Regime classification of an exothermic reaction with nonuniform initial conditions," *Combustion and Flame*, Vol. 39, No. 2, Oct. 1980, pp. 211–214.

[39] Kapila, A. K., Schwendeman, D. W., Quirk, J. J., and Hawa, T., "Mechanisms of detonation formation due to a temperature gradient," *Combustion Theory and Modelling*, Vol. 6, No. 4, Dec. 2002, pp. 553–594.

[40] Sharpe, G. J. and Short, M., "Detonation ignition from a temperature gradient for a two-step chain-branching kinetics model," *Journal of Fluid Mechanics*, Vol. 476, March 2003, pp. 267–292.

[41] Liberman, M. A., Kiverin, A. D., and Ivanov, M. F., "On detonation initiation by a temperature gradient for a detailed chemical reaction models," *Physics Letters A*, Vol. 375, No. 17, April 2011, pp. 1803–1808.

[42] Poland, J. and Kassoy, D. R., "The induction period of a thermal explosion in a gas between infinite parallel plates," *Combustion and Flame*, Vol. 50, Jan. 1983, pp. 259–274.

[43] Radhwan, A. M. and Kassoy, D. R., "The response of a confined gas to a thermal disturbance: rapid boundary heating," *Journal of Engineering Mathematics*, Vol. 18, No. 2, 1984, pp. 133–156.

[44] Clarke, J., Kassoy, D. R., and N. Riley, "Shocks Generated in a Confined Gas Due to Rapid Heat Addition at the Boundary. I. Weak Shock Waves," *Proceedings of the Royal Society A: Mathematical, Physical Sciences*, Vol. 393, No. 1805, 1984, pp. 309–329.

[45] Clarke, J., Kassoy, D. R., and N. Riley, “Shocks generated gas due to rapid heat addition at the boundary. II. Strong Shock Waves,” *Proceedings of the Royal Society A: Mathematical, Physical Sciences*, Vol. 393, No. 1805, 1984, pp. 331–351.

[46] Clarke, J. F., Kassoy, D. R., and Riley, N., “On the direct initiation of a plane detonation wave,” *Proc. Roy. Soc. London A.*, Vol. 408, 1986, pp. 129–148.

[47] Clarke, J. F., Kassoy, D. R., Meharzi, N. E., Riley, N., and Vasantha, R., “On the Evolution of Plane Detonations,” *Proc. Roy. Soc. London A.*, Vol. 429, No. 1877, 1990, pp. 259–283.

[48] Kassoy, D. R., “The response of a compressible gas to extremely rapid transient, spatially resolved energy addition: an asymptotic formulation,” *Journal of Engineering Mathematics*, Vol. 68, No. 3-4, Aug. 2010, pp. 249–262.

[49] Kassoy, D. R., “Non-diffusive ignition of a gaseous reactive mixture following time-resolved, spatially distributed energy deposition,” *Combustion Theory and Modelling*, Vol. 18, No. 1, Jan. 2014, pp. 1–16.

[50] Kassoy, D. R., “Mechanical Disturbances Arising From Thermal Power Deposition in a Gas with Application to Supercritical Liquid Rocket Engine Combustion Instability,” *51st AIAA Aerospace Sciences Meeting*, Vol. 0567, 2013, pp. 1–13.

[51] Regele, J. D., “Effects of Inertial Confinement on the Ignition of Diffusion-Free Unreacted Pockets,” *24th ICDERS*, 2013, pp. 1–6.

[52] Chen, J. H., Hawkes, E. R., Hewson, J. C., Sankaran, R., and Im, H., “The Effect of Turbulent Mixing on Compression Ignition of a Lean Hydrogen/Air Mixture,” *Proceedings of the Western States Section of the U.S. Sections of The Combustion Institute*, 2003, pp. 1–6.

[53] Anderson, J. D., *Modern Compressible Flow*, McGraw Hill, 2nd ed., 1990.

[54] Vasilyev, O. V. and Bowman, C., “Second-Generation Wavelet Collocation Method for the Solution of Partial Differential Equations,” *Journal of Computational Physics*, Vol. 165, No. 2, Dec. 2000, pp. 660–693.

[55] Kevlahan, N. K. R. and Vasilyev, O. V., “An Adaptive Wavelet Collocation Method for Fluid-Structure Interaction at High Reynolds Numbers,” *SIAM Journal on Scientific Computing*, Vol. 26, No. 6, Jan. 2005, pp. 1894–1915.

[56] Regele, J. D. and Vasilyev, O. V., “An Adaptive Wavelet-Collocation Method for Shock Computations,” *International Journal of Computational Fluid Dynamics*, Vol. 23, No. 7, 2009, pp. 503–518.

[57] Kurtz, M. D. and Regele, J. D., “Acoustic timescale characterization of a one-dimensional model hot spot,” *Combustion Theory and Modelling, Accepted*, 2014.

[58] Chui, C. K., *Wavelets: A Mathematical Tool for Signal Analysis*, 1997.

[59] Mallat, S., *A Wavelet Tour of Signal Processing*, Academic Press, 1998.

[60] van Leer, B., “Flux-vector splitting for the Euler equations,” *The 8th Internat. Conference on Numerical Methods for Engineering, Aachen, Germany*, 1982.

[61] Anderson, W. K., Thomas, J. L., and Van Leer, B., “Comparison of finite volume flux vector splittings for the Euler equations,” *AIAA Journal*, Vol. 24, No. 9, Sept. 1986, pp. 1453–1460.

[62] Shu, C.-W. and Osher, S., “Efficient Implementation of Essentially Non-oscillatory Shock-Capturing Schemes,” *Journal of Computational Physics*, Vol. 77, 1988, pp. 439–471.